Probing the Rate of Ca^{2+} Dependent NB Growth and Drugs Response Using Dynamic Mathematical Models

A thesis submitted in the partial fulfillment of the requirement for the degree of MS in Bioinformatics

By

Zoya Amjad

Master of Science in Bioinformatics

Fall 21-MSBI-NUST00000364504

Supervised by

Prof. Dr. Ishrat Jabeen

School of Interdisciplinary Engineering & Sciences (SINES)

National University of Sciences & Technology (NUST)
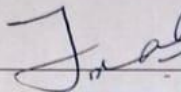
Islamabad, Pakistan

August , 2023

THESIS ACCEPTANCE CERTIFICATE

Certified that the final copy of MS/MPhil thesis written by **Ms. Zoya Amjad, Registration No. 00000364504** of **MS-BI SINES** has been vetted by the undersigned, found complete in all aspects as per NUST Statutes/Regulations, is free of plagiarism, errors, and mistakes, and is accepted as partial fulfillment for the award of MS/MPhil degree. It is further certified that necessary amendments as pointed out by GEC members of the scholar have also been incorporated in the said thesis.
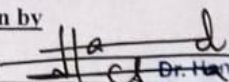
Signature with stamp: _____

Name of Supervisor: <u>Prof. Dr. Ishrat Jabeen</u>

Date: <u>16/08/2023</u>

DR. ISHRAT JABEEN
Professor
School of Interdisciplinary
Engineering & Sciences
NUST Sector H-12 Islamabad

Signature of HoD with stamp: _____

Associate Professor
SINES - NUST, Sector H-12
Islamabad

Date: _____ 17 AUG 2023

Countersign by

Signature (Dean/Principal): _____

Date: _____18/08/2023_____

Dr. Hammad M. Cheema
Principal & Dean
SINES - NUST, Sector H-12
Islamabad

CERTIFICATE OF ORGANILITY

I hereby declare that the research work presented in this thesis has been generated by me as a result of my own research work. Moreover, none of its contents are plagiarized or submitted for any kind of assessment or higher degree. I have acknowledged and referenced all the main sources of help in this work.

Zoya Amjad

Fall 2021-MS BI 0000036450

ACKNOWLEDGMENT

Table of Contents

LIST OF FIGURES

LIST OF TABLE

Abstract

Intracellular Ca^{2+} ($[Ca^{2+}]i$) serves as a critical regulator of various cellular processes and plays a vital role in cellular growth, development, differentiation, and apoptosis. Several studies have reported imbalanced Ca^{2+} expression under pathophysiological conditions, suggesting that targeting $[Ca^{2+}]i$ could be a potential therapy for regulating cellular responses. In this study, we extended the work of Wacquier *et al.*, 2016 and predicted that Ca^{2+} oscillatory patterns in tumorigenic cells exhibit higher Ca^{2+} amplitude compared to normal cells. The predicted Ca^{2+} oscillatory pattern is then incorporated into the cell growth model of Wallace *et al.*, 2016 to observe its effect in both normal and SK-N-SH cells. A combined deterministic model, integrating data from both Ca^{2+} signaling and cell growth, is extended to a 15-day duration to observe the long-term effects of Ca^{2+} oscillation on growth patterns. The graphical illustrations of the simulations reveal the uncontrolled growth of SK-N-SH cells. The model is further modified to predict an optimal treatment protocol to consider the impact of different therapeutic drugs and Ca^{2+} modulators. The model results demonstrated that combined chemotherapy treatments lead to improved outcomes compared to using single chemotherapy. Similarly, the graphical representation of the growth patterns shows the sinusoidal behavior of the curves, indicating that the proposed chemotherapy does not completely eradicate tumorigenic cells but helps maintain the cell count at a reduced level. Our results also highlight the significant influence of Ca^{2+} oscillation on cell count when considering chemotherapeutic treatments.

<div align="right">**Chapter 1**</div>

1 Introduction

1.1 Neuroblastoma

Neuroblastom (NB), a pediatric heterogeneous disease of the sympathetic nervous system, arises in the adrenal glands or in the sympathetic ganglia. NB is the most common fatal disease in infancy with 25-50 cases per million individuals [1]. The common metastatic sites for NB are bone marrow, lymph nodes, bone, liver, and orbital organs. Approximately 15% of all pediatric cancer death are caused by NB. The prognostic factors that determine the risk of disease are the age of the patient at diagnosis, tumor histology, tumor ploidy, recurrent segmental chromosomal copy number alteration, and amplification of proto-oncogene (MYCN). The NB patients are classified into four categories (very low, low, intermediate, and high risk) based on their prognostic clinical and biological features as suggested by the international Risk Group (INRG) [2]. The survival rate of low and intermediate NB patients is 90% and the 5-year survival rate of patients with high-risk NB is less than 50 %. In general, children diagnosed with a localized tumor before one year of age, is curable with surgery or little or no adjuvant treatment. But in those cases where there are extensive hematogenous metastases, most of the patients die despite the extensive treatment [3].

Cancer is mainly caused by the heritable sets of genes that regulate the cell division, differentiation, proliferation, and apoptosis. The underlying genetic factors of NB is the amplification of MYCN, copy number alteration, numerical and segmental chromosomal aberration, mutations and rearrangement in genes such as ALK, ATRX, p53, RAS/MAPK pathway genes, and TERT [4] [5].

1.2 Potential Therapies

The current treatment options available for NB include surgery, radio therapy, chemotherapy, myeloablative chemotherapy with stem cell transplant, biological targeting, and immunotherapy [6]. At present there is no surgical treatment, that can assure the complete resection of the tumor while avoiding damage to the surrounding organs and tissues. It mainly depends on the surgeon's expertise and confidence in the proposed treatment. So more extensive and randomized clinical trials are necessary for the standardized protocol of these tumor treatments [7].

1.3 Late Effects of the Treatment

Survivors of NB experience significant late effects that are directly linked to the severity of their treatment. The incidence and severity of late effects has increased as treatment has become more aggressive. One of the most common side effects is the hearing loss and caused primarily by platinum compound exposure. Up to 73% of the patients are effected by hearing loss[6]. Platinum compounds are responsible for approximately 10-40% of the patients experiencing renal toxicities including hypertension, hematuria, tubular dysfunction, and chronic renal failure. Dental disease is another side effect [8]. High-risk treatment may also cause a range of neurological conditions, from sensory deficits to overt epilepsy. These conditions are directly caused by surgical intervention or radiotherapy.

Musculoskeletal changes such as scoliosis and osteoporosis occur as a result of various endocrine and non-endocrine etiologies, reducing the linear growth of NB survivors[6]. Endocrine system effects mostly seen in the high-risk NB patients and result in growth hormone deficiency, premature ovarian failure, insulin resistance and hypothyroidism. Chemotherapy and radiation therapy effect other organ including pulmonary and cardiac system.

The increased use of many new therapies, such as MIBG therapy, for children with high-risk NB complicates the ability to predict and prevent future side effects. Early research has linked MIBG therapy to new-onset of thyroid dysfunction, myelodysplastic syndrome, and secondary leukemias [9]. In 2-7% NB survivors, high risk therapies are the potential cause of developing a second malignant neoplasm [10]. Alkylating agents, platinum compounds, radiotherapy, and topoisomerase II inhibitors are risk factors for secondary malignancies. Various types of secondary malignancies are observed including thyroid carcinoma, sarcomas, acute myeloid leukemia, renal cell carcinoma and lymphoma. High-risk patients require continuous monitoring and persistent follow-up to avoid the late effect of any therapy. This further necessitates understanding the cell regulation mechanistic of different cellular entities and their impact on the cell response. Which might assist in cellular response mediated potential therapeutic intervention for future therapy.

1.4 Ca^{2+} and Cell Metabolism

Many cells in living organism shows oscillatory behavior, examples include lung respiration, heart beating, sleep-weak cycle, and movement of bird wings and fish trail. Similarly, at microscopic

scales, mechanisms like cell cycle related enzymes, cAMP, or Ca^{2+} concentration within the cell shows the oscillatory behavior. Ca^{2+} oscillations observed in mid-1980s in non-excitable cells, but it has been observed a long time ago in periodically contracting muscles cells, such as heart cells, and in neuron [11]. The oscillation frequency ranges from 10^{-3} to approximately 1 Hz. The detailed process of Ca^{2+} signaling is described in Figure 1.
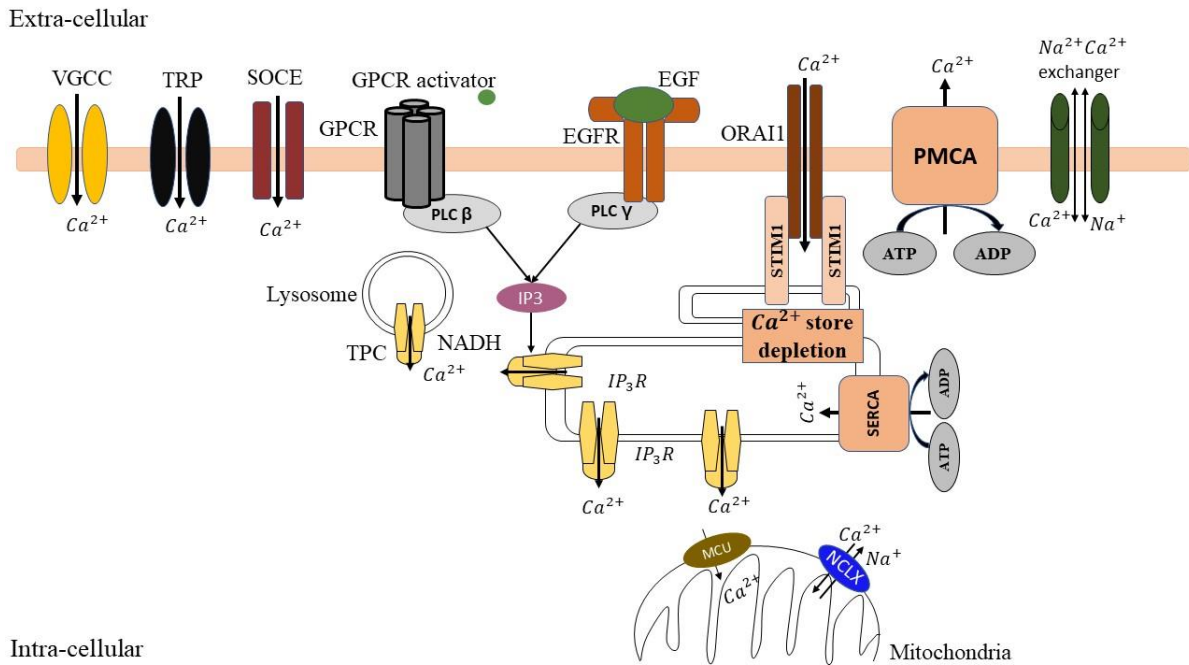
Figure 1. The concentration of Ca^{2+} in the extra-cellular medium is 1mM, much higher than the Ca^{2+} ion concentration within the cytosol,100 nM. The cytosolic Ca2+ increases due to the influx from extra-cellular medium via membrane channels including, VGCC, a membrane Ca^{2+} permeable ion channel, or TRP (transient receptor potential), SOCE, or ROCE, and internal stores including ER/SR and mitochondria. Ca^{2+} release from internal stores mediated by IP_3. IP_3 is produced due to the stimulus from G-protein coupled receptor (GPCR) or the receptor tyrosine kinase including epidermal growth factor receptor (EGFR) by the activation of phosphoinositide-specific phospholipase Cβ (PLCβ) and PLCγ, respectively. The Ca^{2+} channel, RyR, is activated by cyclic ADP lipase. The IPR and RyR are also stimulated by Ca^{2+}, known as Ca^{2+}-Induce-Ca^{2+}-Release (CICR). The store depletion is detected by STIM1 (Ca^{2+} Sensor Stromal Interaction Molecule 1) which in turn activates Ca^{2+} release activated Ca^{2+} channel protein 1 (Orai 1) and initiates the store refilling mechanism by SERCA (Sarcoplasmic/ER Ca^{2+} ATPase) pump. Like SERCA, PMCA is also an ATPase pump. Mitochondria, another important organelle, contributes significantly to the exclusion of Ca^{2+} from the cytosol. The inner mitochondrial membrane contains different transport processes such as permeability transition pores PTP, NA^+/Ca^{2+} and H^+/Ca^{2+} exchangers, and Ca^{2+} uniporters

(MCU) that function as export pathways. The Ca^{2+} released by ER is indeed sequestered by mitochondria. MCU release Ca^{2+} from the cytosol into mitochondria while Na^+/Ca^{2+} and H^+/Ca^{2+} exchanger transport Ca^{2+} against the concentration gradient. Permeability transition pores (PTP) export the Ca^{2+} outside of the mitochondria. Note that some of the transporters have multiple isoforms and not all the Ca^{2+} pumps, exchangers, and ion channels are illustrated here [12].

There is little information available about how cells can exhibit Ca^{2+} oscillation with a period of less than a second while other cells can exhibit such oscillation with a period of hundreds of seconds. This oscillation time can be adjusted by varying the rate at which crucial internal variables move throughout the dynamic structure and the rate at which Ca^{2+} stimulates Ca^{2+} efflux from internal storage and influx from the extracellular region. The bulk of cells' signaling processes, such as gene expression and cell differentiation, can be investigated using changes in oscillation frequency. In other cells, the oscillation frequency is less relevant than the mean Ca^{2+} concentration. It appears that the signal is delivered by a frequency shift rather than the absolute oscillation frequency, resulting in a signaling method that is resistant to intercellular variability, even within the same cell type.

1.5 Intracellular Ca^{2+} Mediated Signaling Pathways and Cellular Responses in NB

In NB, intracellular Ca^{2+} concentration ($[Ca^{2+}]i$) plays a vital role in maintaining cell proliferation, apoptosis, and differentiation. $[Ca^{2+}]i$ within the cell is lower as compared to the extracellular fluid. The signaling pathways involved in NB growth and proliferation are regulated by various growth factors including nerve growth factor (NGF), epidermal growth factors (EGF), vascular endothelial growth factors (VEGF), insulin-like growth factors (IGF), and platelet-derived growth factors (PDGF), as shown in the Figure 2. These growth factors further activate the downstream proteins by intermediate kinases (PI3K/AKT, ALK, and FAK) as well as transcription factors (MCN, NF-KB, and p53). The $[Ca^{2+}]i$ regulates these kinases via the calmodulins and CaM-dependent kinase.
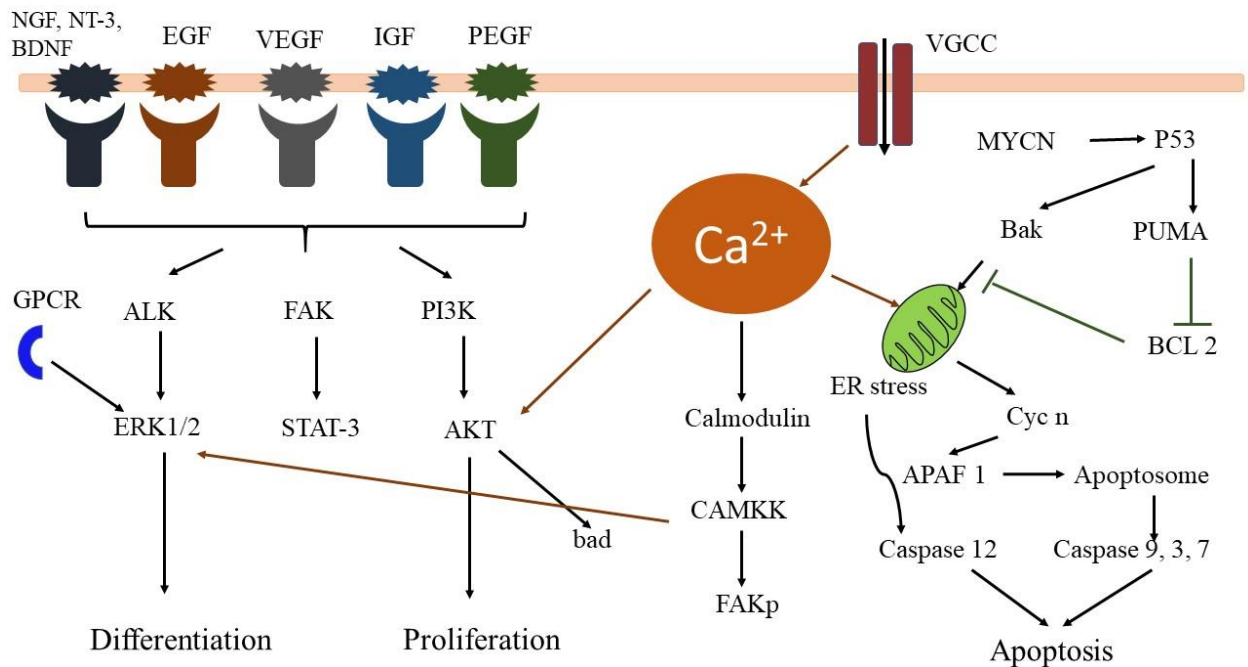
Figure 2: Signaling pathways involved in NB cell's proliferation, differentiation, and apoptosis, the image is taken from [13].

1.5.1 Protein Kinases

PI3K/AKT is the major pathway involve in NB growth [14] and has been described in NB's cell lines (SK-N-BE, SH-SY5Y , SK-N-EP, IMR32, and SK-N-SH) [15]. Different studies reported that by inhibiting the PI3K/AKT pathway, NB cells can undergo apoptosis. The MYCN amplified NB cells showed the greater inhibition of PI3K/AKT, which is thought to be a major factor in NB prognosis. AKT inhibitors such as temsirolimus and perifosine are currently being studied in clinical trials for their safety in children.

ALK (Anaplastic lymphoma kinase) is an insulin receptor that plays a key role in cell growth and development via the central nervous system [16]. The expression of ALK protein was observed in 90% of NB cases and it is associated with the mutation in ALK gene [16]. The downstream signaling cascade of ALK involves AKT, ERK1/2, and STAT3, which are phosphorylated by Ca^{2+} (AKT, ERK, and FAK) and are involved in NB cell survival signaling.

The intermediate kinases involved in cell survival are regulated by $[Ca^{2+}]i$. In NB, NGF signaling is a dominant signaling pathway which is regulated by Trktyrosine receptor family (Trk). TrkA is a receptor of NGF, TrkB for brain-derived neurotrophic factor (BDNF) and TrkC for

neurotrophin-3(NT-3) [17]. Another receptor for NGF is p75^{NTF} but its affinity is less than TrkA. In NB cell lines, NGF signaling leads to the activation of ERK-MAP kinases that exert their role in cell functioning.

ERK signaling cascade is associated with the increase in cellular growth, differentiation, and development. Both the ERK signaling and raised $[Ca^{2+}]i$ are the important regulators for initiation of the intracellular signaling by extracellular ligands. Higher $[Ca^{2+}]i$ initiate the ERK cascade via calmodulin-dependent kinases 1 and 2 [18]. Studies on the PC12 cell line confirm that $[Ca^{2+}]i$ and CAM control ERK activation by NGF signaling [19]. An elevated level of $[Ca^{2+}]i$ activate the CAMPKK which activates the protein kinase B or AKT by phosphorylating the BAD and promote cell proliferation. FAK have an important role in cellular growth and proliferation of NB. $[Ca^{2+}]i$ activates CAMKII which activate the FAK by its phosphorylation.

NB causes occlusions of cell differentiation process. One of the possible treatments is to induce cell differentiation. In NB cell lines, a high level of $[Ca^{2+}]i$ is linked with induction of differentiation. $[Ca^{2+}]i$ of NB cell lines can be increased either through the influx from the extracellular space via VGCC [20] or from intracellular stores with several GPCR ligands. GPCR ligands like retinoic acid, sigma 2 factor, trimethyl-tin chloride (TMT), arsenic trioxide and cisplatin are used to induce apoptosis or cell differentiation [21].

The programmed cell death (PCD) is an important step in cell maintenance, regression, and development. It can be either intrinsic or extrinsic, with both activating caspase 3, 6, and 7, which trigger the DNase and cleave other proteins, resulting in cell death [22]. Membrane induced apoptosis depend on the extracellular ligands including tumor necrosis factors alpha (TNF-alpha) and first apoptosis signal ligands (FAS) and their receptors TNFR and FAS. These receptors induce the death inducing signaling complex (DISC) which stimulate the caspase and activate the executioner caspase 3, 6 and 7. The caspase initiates the cleavage of hundreds of cellular targets.

1.5.2 Ca^{2+} Transport Channels

Intracellular apoptosis also known as mitochondria centered apoptosis. The mitochondrial Ca^{2+} Uniporters (MCU) support the Ca^{2+} uptake and create the negative potential across the membrane which helps to move Ca^{2+} across membrane without the hydrolysis of ATP or transport of other ions. Several mitochondrial proteins are released due to mitochondrial osmotic imbalance and

mitochondrial outer membrane permeabilization. One of the mitochondrial protein, cytochrome c binds with the Apoptotic proteinase activating factors (APAF1) forming the apoptosome, a multi-protein complex, that activate the caspase 3 and 7 which causes apoptosis [23]. Mitochondrial Ca^{2+} overload is another regulatory mechanism of apoptosis. Under stress conditions like hypoxia, unbuffered ROS production, alteration or poising of electron transport chain, and imbalance mitochondrial protein hemostasis leads to the opening of mitochondrial transition pores (MTP). Due to the opening of permeability transition pores several apoptogenic factors are released. Cancer cells can evade apoptosis by downregulating Ca^{2+} signaling necessary to start the apoptotic mechanism. The release of Ca^{2+} from ER regulates mitochondrial apoptosis [24]. BCL-2 protein members control apoptosis and cell growth, by altering the release of ER-Ca^{2+} into mitochondria.

P53, a tumor-suppressive protein, causes the inactivation of tumorigenesis. In NB with MYCN-amplified cell lines, p53 initiates cell apoptosis and is a direct transcriptional target of MYCN [25]. By turning on the pro-apoptotic targets Bax and PUMA, which are transactivated by p53, MYCN also triggers apoptosis.

1.6   Intracellular Ca^{2+} Modulation with Chemotherapy Drugs

Different chemotherapeutic drugs modulate the $[Ca^{2+}]i$ including cisplatin (CDDP), arsenic trioxide (As_2O_3), and tri-methyl-tin chloride (TMT). These drugs induce apoptosis by meddling with $[Ca^{2+}]i$ hemostasis. Cisplatin is one of the most efficacious chemotherapies for NB. Cisplatin's anti-therapeutic role is induced by cytotoxicity and apoptosis (increased caspase 8 and 9 activity) [26]. Cisplatin combines with Ca^{2+} signaling, p53, ROS, and apoptosis by increasing caspase 8 and 9 activities and increasing p53 expression. The studies showed that the increase in $[Ca^{2+}]i$ is dependent on CDDP concentration. CDDP induces apoptosis by activating calpain, which is controlled by inositol triphosphate IP_3. The increase in $[Ca^{2+}]i$ concentration due to the activation of IP_3 increases the efficacy of cisplatin thus increasing the apoptosis. Cisplatin-induced Ca^{2+} influx through the IP_3 receptors induces cellular apoptosis via calpain activation rather than caspase-8 activation, showing that cisplatin-induced Ca^{2+} influx through the IP_3 receptors induces cellular apoptosis through calpain activation [27].

Table 1: Increase of $[Ca^{2+}]i$ in NB cell line in human due to two main types of receptors, G protein-coupled receptor (GPCR) and sigma factor 2 [13] via IP_3. IP_3 is produced due to the stimulus from GPCR by the activation of phosphoinositide-specific phospholipase Cβ (PLCβ).

Sr. no.	Treatment	Cell line	Receptor	Ca^{2+} release	Basal $[Ca^{2+}]$	Increased $[Ca^{2+}]$
1	Oxotremorine-M	SH-SY5Y	Muscarinic Receptor (GPCR)	Store Release(IP_3R)	50nM	2-fold
2	Methacholine	SH-SY5Y	Muscarinic Receptor (GPCR)	Store Release (IP_3R)	98 nM	2-fold
3	Carbachol	SH-SY5Y	Muscarinic Receptor (GPCR)	Store release	--	2.5-fold
4	Carbachol	SK-N-SH	Muscarinic Receptor (GPCR)	Store release	59nM	2-fold
5	Bradykinin	SH-SY5Y	Bradykinin receptor (GPCR)	Store release (IP_3R)	98nM	1-fold
6	Bradykinin	SH-SY5Y	Bradykinin receptor (GPCR)	Store release	--	2-fold
7	Orexin-A(GPCR)	IMR-32	Orexin type 1 receptor (GPCR)	Store release(IP_3R)	50nM	4-fold
8	Retinoic acid	SH-SY5Y	Retionic X receptor	Store release	98nM	No increase

...

			(Nuclear Receptor)			
9	Retinoic acid	SH-SY5Y	Retionic X receptor (Nuclear Receptor)	Store operated Ca^{2+} channel	10nM	4-fold
10	Arsenic trioxide	SH-SY5Y	--	Store operated(IP_3R and RyR)	75nM	2-fold
11	Trimethyltin	SH-SY5Y	--	Store release (IP_3R and RyR)	--	2-fold
12	Chloride	SH-SY5Y	--	Store release	--	2-fold
13	Cisplatin	SH-SY5Y	--	Extracellular space	75nM	2-fold
14	Ibogaine	SK-N-SH	Sigma 2 receptor	Thapsigargin insensitive Ca^{2+} store	--	1-fold
15	Haloperidol	SK-N-SH	Sigma 2 receptor	Thapsigargin insensitive Ca^{2+} store	--	1-fold
16	BD1008	SK-N-SH	Sigma 2 receptor	Thapsigargin insensitive Ca^{2+} receptor	--	1-fold
17	LR172	SK-N-SH	Sigma 2 receptor	Thapsigarian insensitive receptor	--	1-fold

18	BD737	SK-N-SH	Sigma 2 receptor	Thapsigarian insensitive receptor	--	1-fold
19	JL-II-147	SK-N-SH	Sigma 2 receptor	Thapsigarain insensitive Ca^{2+} receptor	--	2-fold
20	CB-64D	SK-N-SH	Sigma 2 receptor	Thapsigarian insensitive Ca^{2+} receptor	--	4-fold

1.7   Mathematical Model

The Ca^{2+} toolbox is used to determine the frequency of the oscillations of Ca^{2+} signaling. It includes Voltage-gated channels, ATPase pumps, and Ca^{2+} channels in the endoplasmic/sarcoplasmic reticulum (ER/SR) membrane. Cells can adjust Ca^{2+} concentration by modifying the spatial and temporal expression of these components [28]. These complex cell signaling mechanisms can be explained using interaction diagrams or cartoon models that depict the set of components and how they interact. The disadvantage of these models is that they include ambiguous information on system behavior, particularly when the interaction network includes feedback. Classical dynamic simulation or quantitative models can be used to gain an *in-silico* understanding of these processes. Classical dynamic simulation is a collection of software programs used to simulate an entire network. Because these interaction diagrams contain a large number of elements, the simulation of these networks is a time-consuming and computationally expensive operation. Mathematical or quantitative models also have the potential to generate intricate signaling mechanisms.

Due to the availability of experimental observation in system biology, mathematical modelling can be utilized to examine intracellular processes. Mathematical modelling is a generalization of reality that focuses on specific elements of the designed objects while removing others. The resulting dynamical mathematical model is made up of equations that describe how the system changes over time. These models aid in simulation by predicting system behavior under

specific conditions and are also used to analyze possible system behavior. These models will never be able to replace lab tests, but they can be used to forecast system behavior that cannot be predicted in the lab. Model simulation provides results in less time compared to classical dynamic simulation and at no real cost, as well as allowing us to investigate circumstances that could never be achieved in the lab. Furthermore, model analysis assists us in understanding why the system performs the way it does, so providing a link between the system and its behavior.

1.8   Problem Statement

In NB, intracellular Ca^{2+} plays a vital role in maintaining cell's proliferation, differentiation, and apoptosis. Excess Ca^{2+} intake in cells due to GPCR may promote cell proliferation and apoptosis under pathophysiological conditions. By maintaining the intracellular Ca^{2+} concentration, the uncontrolled cellular division can be controlled. In the current research, a mathematical model is proposed to predict the effect of Ca^{2+} on the rate of tumor growth and subsequently the impact of different chemotherapeutic drugs on respective tumor growth and inhibition. The generated quantitative model could help us in comprehending the disease's complex dynamics and probing the effective regulating or therapeutic mechanism. These models will forecast the drug concentration and schedule necessary for a timely and efficient treatment.

1.9   Objectives

The objectives of this study is the use of Mathematical models:

a. To analyze the dynamic of NB.
b. To evaluate the effect of perturbed and normal Ca^{2+} intake on NB growth.
c. To demonstrate the effect of different chemotherapeutics and Ca^{2+} regulators on NB growth and inhibition.
d. To predict the optimized dosage against NB.

<div align="right">**Chapter 2**</div>

2   Literature Review

2.1   Ca²⁺ Signaling

Ca^{2+} physiology is a vast field and has a crucial role in maintaining cellular physiology. Ca^{2+} in every cell exhibits complex spatiotemporal behavior, including scholastic spiking, regular Ca^{2+} oscillation, periodic waves, and spiral oscillations. These waves control the majority of cellular functions. Total Ca^{2+} in the human body weight around 1300g, and 99% is located in bones, 0.1% in extracellular fluid (ECF), and 1% in cells. Three hormones: calcitonin, parathyroid hormone (PTH), and calcitriol, are responsible for controlling the flow of Ca^{2+} between these compartments as well as its secretion and excretion, shown in Figure 3. PTH, which is produced by the parathyroid gland, increases the kidney's ability to reabsorb Ca^{2+} from the bones and stimulates the creation of calcitriol. The proximal tubules of the body produce the hormone calcitriol, which boosts gastrointestinal intake of Ca^{2+} and promotes bone resorption. Calcitonin increases the Ca^{2+} movement into the bones. All three inhibit Ca^{2+} excretion from the kidney by promoting reabsorption [29] [30].

Intracellular Ca^{2+} concentration regulates cellular processes like cell growth, differentiation, and metabolism. The ECF has a Ca^{2+} concentration of 1mM while plasma membrane pumps, exchangers, and internal stores maintain a lower range of cytosolic Ca^{2+} concentration of around 0.1µM. A small influx either from external pumps/channels or internal stores causes a rapid increase in Ca^{2+} concentration therefore, the concentration of Ca^{2+} in the cytosol is tightly maintained. Cells need to expand a considerable amount of energy to maintain a reasonable amount of Ca^{2+} concentration for normal physiology. Long-term, elevated intracellular Ca^{2+} concentration is extremely hazardous. One of the reasons is that in cells, it controls various effectors molecules like kinases and phosphatases which control a number of critical activities, including cell proliferation, secretion, differentiation, apoptosis, and gene transcription.

Ca^{2+} as a secondary messenger controls a wide number of cellular functions. It regulates the coupling of excitation and contraction in muscle cells, secretion and stimulation at synapses, and fluid transport in exocrine epithelia. It functions in gene regulation and cell type differentiation, regulates plasticity in pre- and post-synaptic neurons, and is crucial for cell mobility [31].
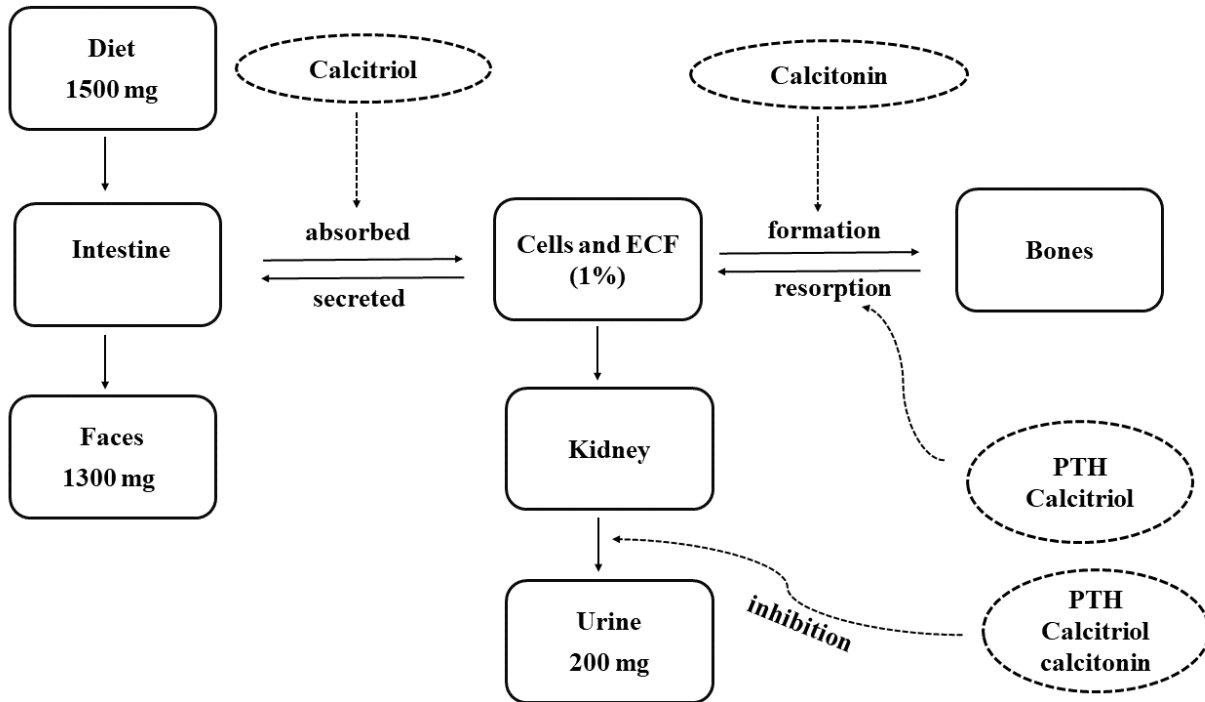
Figure 3. Ca^{2+} hemostasis in whole body. Most of the Ca^{2+} absorbed in bones with only 1% in extracellular fluid. The movement of Ca^{2+} across intestine, ECF, and bones is regulated by three hormones, that is, Calcitonin, PTH, calcitriol [32].

2.2 Ca^{2+} and Metabolism in Cancer

Ca^{2+} as a secondary messenger involved in many metabolic pathways, a term named as 'Ca^{2+} transportome', refer to the channels and transporter involved in efflux and influx of Ca^{2+} across the membrane as well as internal stores such as endoplasmic/sarcoplasmic reticulum and mitochondria. After the influx of Ca^{2+} into the cell, the SERCA pump causes the Ca^{2+} to move into the ER/SR and similarly the receptors present on the surface of ER/SR, that is, IP$_3$R and RyR

moves the Ca^{2+} out of the internal store. The Voltage dependent anion selective channel protein (VDAC) and the Mitochondrial Ca^{2+} uniporter (MCU) protein transport Ca^{2+} into the mitochondria. Elevated Ca^{2+} in the cytosol regulates and activates various Ca^{2+} binding proteins, enzymes, transportome activities, and gene expression.

Ca^{2+} pumps and transporters have a wide range of tissue dispersion and selectivity. Abnormal expression of these pumps and channels, as well as other Ca^{2+} binding proteins (such as STIM, Calpains, Calmodulin, TRPM, and calnexin), has been linked to the start and progression of various cancer types.

Changes in Ca^{2+} concentration govern the signaling pathways and metabolic processes that control cell proliferation and cell cycle in cancer cells. Different transcription factors (such as cAMP response element binding protein CREB, nuclear factor of activated T cells NFAT-1, and Activating transcription factor-1 ATF-1) and oncogenes such as MYC, FOS, and JUN control the expression of CDKs and cyclin [33]. The passage through the G1/S checkpoint is caused by the activation of CDK complexes. These nucleus transcription factors are activated by calcium. Localized Ca^{2+} entry via calmodulin, ERK, and GPCR all play key roles in cell proliferation. Ca^{2+} phosphorylates retinoblastoma protein, a transcription factor involved in the G1-S shift. Calmodulin kinase is responsible for the G2/M shift, is also regulated by Ca^{2+} [34].

The quantity of Ca^{2+} in the ER and mitochondria regulates cell apoptosis. In cancer cells, apoptosis is prevented by various pre-apoptotic (bad, bax, and bak) and post- apoptotic (bcl-xl/bcl-2) markers. Bad is phosphorylated by PKA, MAPK, or PKB, which causes it to dissociate from mitochondria and attach to the 14-3-3 protein. Bad is unable to suppress bcl-xl/bcl-2 after binding and thus promotes apoptosis [35]. In contrast, calcineurin dephosphorylates bad, causing it to bind to bcl-xl/bcl-2 and prevent apoptosis. Ca^{2+} transport proteins like IP$_3$R, SERCA, MCU, and PMCA are also influenced by pro- and anti-apoptotic factors. These apoptotic proteins control the IP$_3$R and SERCA, reducing Ca^{2+} uptake by mitochondria and Ca^{2+} release from the ER membrane. This signaling mechanism could decrease calcium-mediated cell death and eventually lead to apoptosis resistance [36].

Ca^{2+} signaling also helps in Tumor cell angiogenesis. The SOCE component proteins Orai and STIM1 mediate vascular endothelial growth factor (VEGF), which triggers cancer cell migration and angiogenesis [37]. By phosphorylating PLC-gamma, the VEGF factor induces the production of DAG and inositol 1,4 5 triphosphate (IP_3). Increased IP_3 levels enhance signal transduction via the MPAK-regulated pathway [38]. Similarly, activation of transient receptor potential cation channel 4 (TRPV4) by basic fibroblast growth factor (BFGF) induces endothelial cell proliferation, migration, and angiogenesis via Ca^{2+} influx [39].

The activation of SOCE by a hypoxic tumor microenvironment increases the expression of hypoxia inducible factor-1 (HIF-1) which supports the expression of angiogenic factors such as stomal-derived factor, angiopoietin-2, and placental growth factor. Upregulated HIF-1 promotes tumor growth by increasing STIM1 expression, which enhances HIF-1 transcription [40]. By regulating nuclear factor k beta (NF-kB) and the production of reactive oxygen species, this pathway promotes tumor progression [41].

Tumor associated macrophages (TAM) promote tumor development by synthesis of the calcium-dependent chemokine ligand 18. TAM also aids tumor cells in evading the defense system [42]. Cytokines and chemokines are released by T cells and macrophages via STIM1 and ORAI1, which are SOCE components. These channels also help $CD4^+$ and $CD8^+$ T lymphocytes differentiate [43].

2.3 Ca^{2+} Signaling Toolbox

The Ca^{2+} signaling toolbox include the following components [44]. The Modeler can construct the model by picking which component to include.

G Protein-Coupled Receptors (GPCR)

Ca^{2+} signaling in many cells begins with the binding of an agonist to a GPCR, present on the surface of the membrane. The agonist binds to the receptor, triggering various signaling pathways over timescales varying from milliseconds to hours. Linderman provided a thorough and comprehensive discussion of GPCR (15). Mahama and Linderman developed a simpler model for GPCR in which the agonist binds to the receptor and forms an agonist receptor complex [45]. The model equation of the complex formation is:

$$A + R \overset{k_1}{\underset{k_{-1}}{\longleftrightarrow}} R^*$$ 2.1

Where R shows the receptor bound to the agonist A to form complex R^*. The differential equation for this reaction is represented as:

$$\frac{d[R^*]}{dt} = k_1[R][A] - k_{-1}[R^*]$$ 2.2

Assuming that the total amount to receptor R* is fixed.

$$\frac{d[R^*]}{dt} = k_1([R]tot - [R^*]) - k_{-1}[R^*]$$ 2.3

This is the basic model of receptor activation, ignoring receptor dimerization, diffusion, conformational changes and binding to other molecules. More detailed work on GPCR is presented by Falkenburger et at. [46] [47], shown in Figure 4. The model equation and parameters are present in the original paper of Falkenburger presents the six states, between the ternary complex model and cubic ternary complex model. The ternary complex model presented by De Lean et al. [48], assuming the receptor can reside in one of the four states: R (the base form), RG (Receptor bound to the G protein), RA (Receptor bound to the agonist) or RGA (Receptor bound to the agonist and G protein). Weiss et al. further extended this model to the cubic ternary model, which has eight states [49]. According to this model, a receptor may be in an active or inactive condition depending on whether an agonist A and G protein are bound or not. The equations of Falkenburger et al. model is then compared with the experimental data, where an optimum concentration of agonist is applied (10 μM Oxo-M).
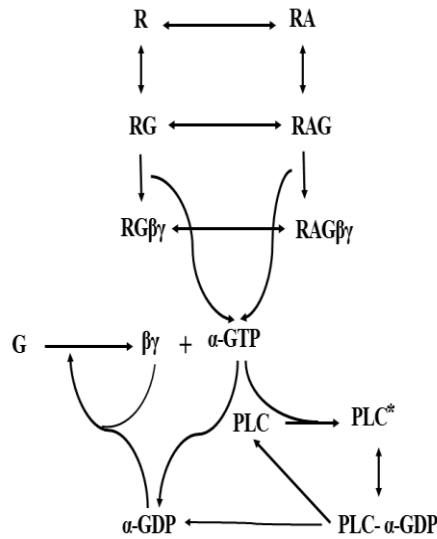
Figure 4. A systematics diagram for GPCR activation. Activated receptor R* binds with G protein and dissociates into βγ and α-GTP. The α-GTP then binds with PLC to form an activated PLC*. The activated PLC by the hydrolysis of α-GTP dissociates into PLC and α-GDP. The α-GTP can be directly hydrolyzed to α-GDP which then reassociate with βγ subunit to reform the inactivated G protein. PLC- α-GDP intermediate complex exist after GTP has been converted to GDP, but before the intermediate complex dissociate.

Another model presented by Lemon et al. also included the desensitization and recycling of the receptor [50].

SERCA and PMCA Pump

SERCA and PMCA are the Ca^{2+} ATPase efflux pathways in Ca^{2+} signaling toolbox. Since both these models are not identical ATPase, it's difficult to make difference between these two pathways. SERCA pump transfer 2 Ca^{2+} ion from cytosol to ER/SR at each ATP consumption [51].The simplest equation based on law of mass action would be:

$$2Ca^{2+}(cyt) + E \overset{k}{\to} 2Ca^{2+}\ (ER) + E \qquad\qquad 2.4$$
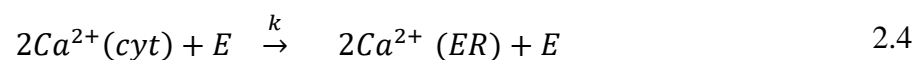
The differential equation will be:

$$\frac{dc}{dt} = -2k[E]c^2 = -\tilde{k}c^2 \qquad\qquad 2.5$$

Where E shows the SERCA pump, and c denotes the cytoplasmic Ca^{2+}. For convenience, modeler equation can be written as:

$$J_{serca} = -\tilde{k}c^2 \qquad\qquad 2.6$$

Where J_{serca} denotes the Ca^{2+} flux due to SERCA pump. One disadvantage of this flux is that it cannot saturate as c rises, which is not physiological. Another model presented by Kenner and Snyed [52], where they use Michaelis-Menten theory of enzyme reaction.

$$2Ca^{2+}(cyt) + E \overset{k_1}{\leftrightarrow} C \overset{k_2}{\to} 2Ca^{2+} (ER) + E \qquad\qquad 2.7$$
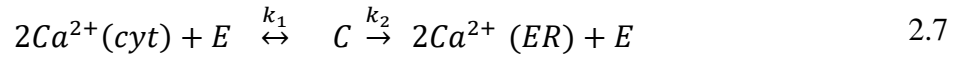
Where C is an intermediate complex formed when cytoplasmic Ca^{2+} binds with pump, and dissociate to release Ca^{2+} into ER/SR. The differential equations of the following equation will be:

$$\frac{dc}{dt} = 2k_{-1}\gamma - 2k_{-1}ec^2 \qquad\qquad 2.8$$

$$\frac{de}{dt} = k_{-1}\gamma - k_1 ec^2 + k_2\gamma \qquad\qquad 2.9$$

$$\frac{dc_e}{dt} = 2k_2\gamma \qquad\qquad 2.10$$

Where c_e is concentration of Ca^{2+} is ER/SR, e denotes [E], and γ denotes the concentration of intermediate complex [C]. The Michaelis-Menten enzymatic reactions are based on either the equilibrium approximation or the quasi-steady-state estimates [52]. The flux obtained by applying the equilibrium approximation to the enzymatic reaction of the SERCA pump would be:

$$J_{serca} = \frac{e_{tot}k_4 c^2}{c^2 + K^2} \qquad\qquad 2.11$$

$e_{tot} = e + \gamma$ is total concentration of SERCA. This equation is called Hill function, has a positive cooperativity. In general, the Hill function is used to describe enzymatic reactions that exhibit cooperative behavior. One drawback of this model is that it does not include the bidirectionality of the ATPase pump; as Ca^{2+} concentrations in the ER rise, the net pump flux falls

to zero. One method for making the pump bidirectional is to include the reverse reactions, in this case the flux would be:

$$J_{serca} = e_{tot} \frac{k_1 k_2 c^2 - k_{-1} k_{-2} c_e^2}{k_1 c^2 + k_{-1}} \qquad 2.12$$

Another method for making pumps reversible is to use the Markov model developed by MacLennan et al. [51]. The schematic diagram is presented in the Figure 5.
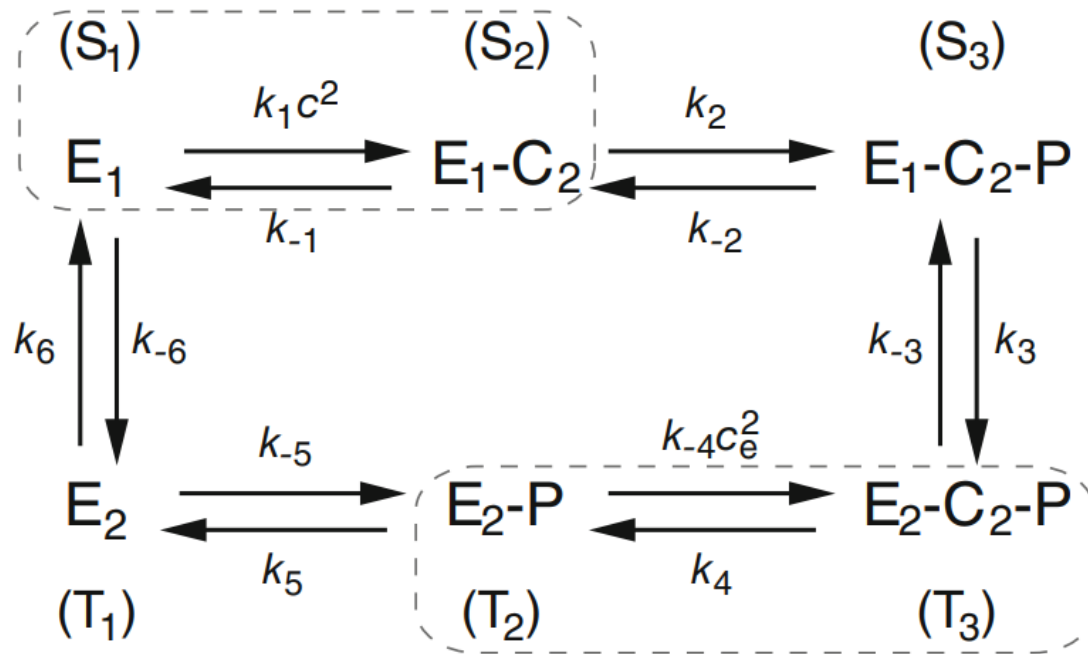
Figure 5. The pump present in two basic conformation E1 and E2. In E1 conformation, the pump binds with two Ca^{2+} ions and after its phosphorylation, it switches to E2 state where Ca^{2+} binding site is exposed to RE lumen. The Ca^{2+} is released into the ER, dephosphorylation occur, and pump switches back to E1 conformation. MacLennan assumed that binding and release of Ca^{2+} occur quickly, so both states S1 and S2 are grouped together with a dotted box. For each transition, the whole process repeated. The differential equation and parameters values are given is original paper [51].

Since SERCA and PMCA are ATPase pumps, two H^+ ions are transported in the opposite way for each Ca^{2+} transfer. The inclusion of these factors results in enormous complexity.

However, Trans et al. [53] reduced a pH and ATP-dependent model of the SERCA pump from 12 to 3 states without losing the model's capacity to replicate the data of Ji et al [54].

Sodium Ca²⁺ Exchanger NCX

The Na^+/Ca^{2+} exchanger is referred to as an active pump because it uses the Na^+ concentration gradient to move Ca^{2+} out of the cell. The Na^+/Ca^{2+} exchanger is an essential transport mechanism in many cells, including neurons and cardiac ventricular cells. In these cells, Ca^{2+} enters by the action potential is removed by the cell through Na^+/Ca^{2+} exchanger. Different models are present to show the transport mechanism of Na^+/Ca^{2+} exchanger [55] [56]. NCX, like SERCA pump, is available in two forms: unidirectional with two substrates as shown in Figure 6, one is cytosolic Ca^{2+}, and other is exterior Na^+. Another option is the bidirectional Markov model.
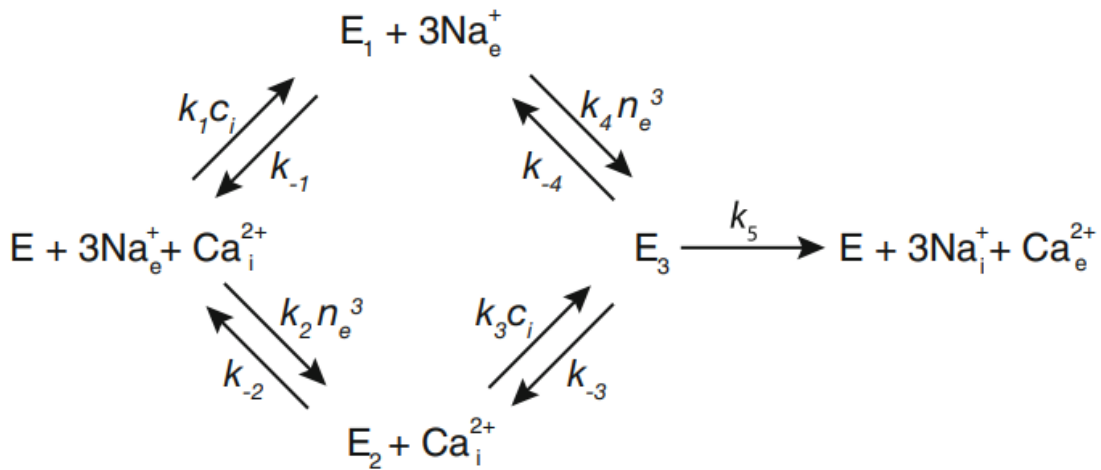
Figure 6. Shows the schematic diagram for unidirectional NCX. ci is cytosolic Ca^{2+} concentration, ne shows the extracellular sodium concentration. E1 is the state where complex has one bound calcium, E2 state has 3 Na^+ bound, E3 state has one Ca^{2+} and three Na^+ bound.

The flux through NCX is as follow:

$$J_{NCX} = V_{max} \left(\frac{c_i}{K_1 + c_i} \right) \left(\frac{n_e^3}{K_2 + n_e^3} \right)$$

2.13
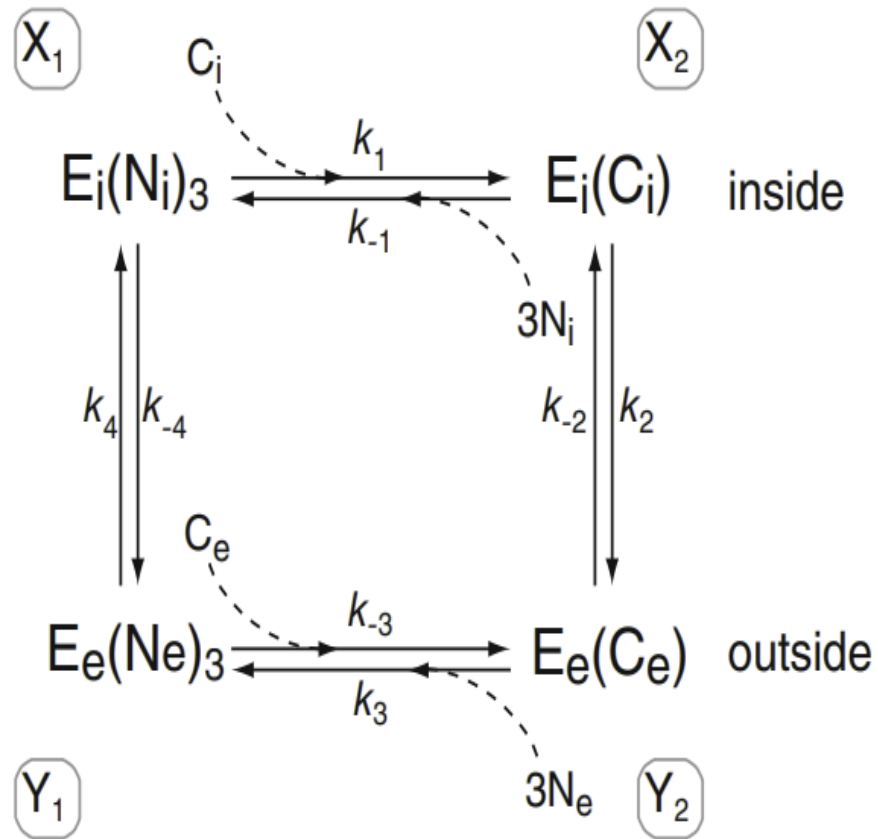
Figure 7: Bidirectional NCX Markov model

NCX can also be represented as a bidirectional Markov model, as shown in the Figure 7, where Ei represents the conformation of exchanger protein exposed to the interior side of the cell and Ee represents the conformation of protein exposed to the exterior side of the cell. In the X1 condition, the exchanger protein binds to one Ca^{2+} ion inside the cell and releases three Na^{+}. When the exchanger's conformation changes to Ee, it releases Ca^{2+} to the outside and bonds with three external Na+. The cycle is completed when the conformation changes to the Ei condition. The flow through NCX is calculated as follows:

$$J_{NCX} = k_4 y_1 - k_{-4} x_1$$

$$\Rightarrow \frac{c_i n_e^3 - K_1 K_2 K_3 K_4 c_e n_i^3}{\beta_1 c_i + (\beta_2 + \beta_3 c_i) c_e + (\beta_4 + \beta_5 c_e) n_i^3 + (\beta_6 + \beta_7 c_i + \beta_8 n_i^3) n_e^3}$$

2.14

Where $Ki = k_{-1} / ki$. NCX is measured in 1/time. This is due to the fact that the variables xi and yi are the probabilities (fractions) of the exchanger in a given state, rather than the number of exchangers in a given state. In this case, the flux is the number of times the exchanger repeats the cycle per unit time. If the exchanger concentration is known, it can be transformed to concentration per time.

The NCX is electrogenic, generating an electric current, by transferring two positive charges out and three positive charges in at each cycle. This demonstrates that a portion of the rate constant must be a function of membrane potential. Consider NCX, where the reaction starts with 3 Na^+ outside the cell and 1 Ca^{2+} ion inside and lasts with 3 Na^+ inside and 1 Ca^{2+} ion outside the cell.

$$3\ Na_e^+ + Ca_i^{2+} \rightarrow 3\ Na_i^+ + Ca_e^{2+} \qquad 2.15$$
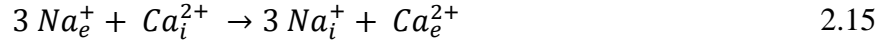
The change in free energy of this reaction is (for more detail see [52]).

$$\Delta G = RT ln \left(\frac{n_i^3 c_e}{n_e^3 c_i} \right) + FV \qquad 2.16$$

At equilibrium, $\Delta G = 0$, in this case,

$$\frac{n_{i,eq}^3 c_{e,eq}}{n_{e,eq}^3 c_{i,eq}} = \exp\ \left(-\frac{FV}{RT} \right) \qquad 2.17$$

According to the principle of detailed balance, the rate of forward reaction is equal to rate of reverse reaction. We get,

$$K_1 K_2 K_3 K_4 = \exp\ \left(\frac{FV}{RT} \right) \qquad 2.18$$

For NCX, a net transfer of one positive charge into the cell is equal to the transfer of one negative charge out of the cell. The flux through NCX is given as.

$$J_{NCX} = \frac{c_i n_e^3 -\ \exp\left(\frac{FV}{RT}\right) c_e n_i^3}{\beta_1 c_i + (\beta_2 + \beta_3 c_i)c_e + (\beta_4 + \beta_5 c_e)n_i^3 + (\beta_6 + \beta_7 c_i + \beta_8 n_i^3)\ n_e^3} \qquad 2.19$$

Mitochondria

Mitochondria, an intracellular Ca^{2+} store, receive Ca^{2+} via Uniporters (MCU) and discharge Ca^{2+} into the cytosol via NCX, a membrane NCX isoform. The energetic balance of mitochondria is tightly regulated by the cell's Ca^{2+} homeostasis. There is little research on the function of Ca^{2+} signaling in mitochondria. According to the present count, mitochondria are most likely to regulate Ca^{2+} signaling in microdomains, a region between the ER and the mitochondria [28] [57]. Mangus and Keizer presented the first mitochondrial model [58] which was later described in detail [59]. Recent studies on mitochondria include a model presented by Cortassa et al. [60], and Nguyen and Jafri [61] with a particular focus on cardiac cells, while Patterson et al. investigated the effect of Ca^{2+} fluxes from the ER, mitochondria, and from the outside [62]. Marhl et al. studied the involvement of mitochondria in complex Ca^{2+} oscillation [63].

Ca^{2+} uptake in mitochondria occurs via mitochondria Ca^{2+} uniporters (MCU), sensitive to the Ca^{2+} concentration on the cytosolic side, and the potential difference across the inner mitochondrial membrane, indicated by the symbol ψ, drives the current through this channel. Potential difference (ψ) $= V_{in} - V_{out} = -180$ mV, and according to the Nernst equation, the Ca^{2+} would continue to penetrate across the membrane until the cytosolic to mitochondrial ratio is approximately 10^{-6}. The uniporter alone would produce a concentration of 100nM in the mitochondria at a cytosolic concentration of 100nM. Since the uniporters open when cytosolic Ca^{2+} concentration is high, this shows that uniporters rely on the spatially restricted Ca^{2+} micro-domain [64]. Uniporters are ion channels that open as a result of ligand binding, which is in this case is Ca^{2+}. The flux through uniporters is defined as the product of two terms: the open probabilities of uniporters and flux through uniporters when they are open.

$$J_{uni} = Ng(c)\emptyset(\psi, c) \qquad\qquad 2.20$$

Here *N* denote the number of uniporters, *g* shows the fraction of uniporters that are open. g can be a function of Numerous factors including potential difference across the membrane or the concentration of ligand. $\emptyset$ denotes the current through single open channel. The current through single open channel can be modelled in different ways, one is Goldman-Hodgkin-Katz (GHK) [52]. The equation gives a simple model of uniporters, similar to the model constructed by Magnus and Keizer [58].
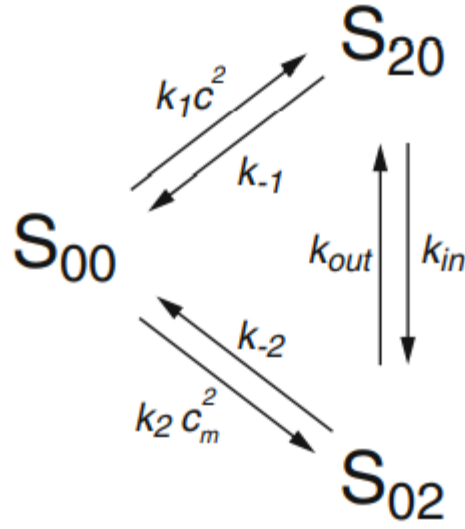
Figure 8. Model of uniporters presented by Dash et al. there is three states of uniporters: first S00, no Ca^{2+} bound, S20, two Ca^{2+} binds to the cytoplasmic side, and S02, two Ca^{2+} bounds to the mitochondria side. C denotes the concentration of Ca^{2+} in the cytoplasm, while cm shows the concentration of Ca^{2+} in mitochondria. S00 is supposed to be in equilibrium with respect to two other states.

Figure 8 shows another model of uniporters given by Dash et al. [65], where they merged the barrier model of ion channel and the Markov model of channel activation. Model equations and parameters are discussed in detail in original paper.

The mitochondrial Na^+/Ca^{2+} exchanger (NCLX), an isoform of NCX of the plasma membrane, works in a similar fashion. The exchanger works as ratioanl function of sodium and Ca^{2+} ion in cytoplasm and mitochondria. Wingrove and Gunter [66] provided an early model of NCXL by fitting their experimental results to a unidirectional enzyme model. The Flux through the channel is given as:

$$J_{NCXL} = V_{max} \left(\frac{c_m}{K_c + c_m} \right) \left(\frac{n_c^2}{K_n^2 + n_c^2} \right) \qquad 2.21$$

Where n_c is Na^+ cytosolic concentration. Magnus and Keizer [58] also uses this expression to studied the flux changes with the inner membrane potential difference by multiplying voltage dependent pre factor with flux equation. The recent studies presented by Nguyen and Jafri [61], Dash and Beard and Pardhan at al. [67] have use the reversible NCX model.

Receptor Operated Ca^{2+} Channel (ROCC)

Ca^{2+} entry through ROCC is supposed to be an increasing function, a linear function, of agonist concentration. Flux through channel is:

$$J_{in} = \propto_o + \propto_1 S \qquad\qquad 2.22$$

Where *S* is the agonist concentration. For models having GPCR activation, the influx could be considered as a linear function of G protein activation [68].

Voltage-Gated Ca^{2+} Channels (VGCC)

One of the most important pathways for Ca^{2+} flux is the VGCC, present in different cell types such as in cardiac cells, the flux of Ca^{2+} from the L-type voltage channel causes the release of Ca^{2+} from SR, which causes contraction. Different types of VGCC are present such as N-type, R-type, L-type, P/Q-type, and T-type. L-type VGCC is present mainly in cardiac, smooth, and skeletal muscle cells. On the base of α1 subunits, the VGCC is described precisely. The L-type channel includes Cav1.1-Cav1.4, similarly, N, P/Q, and R-type include Cav2.1-Cav2.3, respectively, and T-type channels include Cav3.1 – Cav3.3 [69]**.** The underlying model structure for different types of VGCC models is similar, only the choice of different parameters shows their different behavior.

The equation for the simplest model of VGCC is:

$$I_{Ca} = N_{Ca} g_{Ca}(V, t) \emptyset(V, c) \qquad\qquad 2.23$$

Where N_{ca} is the total number of channels, *V* is the membrane potential, *gca* denotes the open probability of a single channel, *c* is the [Ca^{2+}]i, and $\emptyset$ denotes the current through a single open channel.

A model example for electrical bursting in pancreatic beta cells was modeled by Chay and Keizer [70] in a similar way as the Na$^+$ channel was modeled by Hodgki and Huxely. They put $g_{Ca}(V, t) = g_{Ca} m^3 h$, where h and m satisfy the equation in Hadgki-Huxely model, and $\emptyset = V - V_{Ca}$, where V_{Ca} is the Ca^{2+} Nernst potential. This approach with minor adaptation was widely used by many other researchers. Another example of the neuroendocrine model, modeled by LeBeau et al. [71] studied the bursting in GTI neurons. They modeled the two Ca^{2+} currents, a T-type current is modeled as:

$$I_{CaT} = g_{Ca,T} \, m_{Ca,T}^2 \, h_{ca,T}(V - V_{Ca}) \qquad\qquad 2.24$$

And an L-type current is modeled as

$$I_{CaL} = g_{Ca,L} \, m_{Ca,L}^2 \, h_{ca,L}(V - V_{Ca}) \qquad\qquad 2.25$$

In their model, the T-type VGCC channel inactivates, while L-type VGCC does not.

The model built by Destexhe and Huguenard [72], used a similar expression for their model of T-type VGCC, the only difference is that they used the GHK expression for $\emptyset$, as compared to the linear expression used by LeBeau et al. [71]. A lot of literature is present on how to model the I-V curve, $\emptyset(V)$ for Ca^{2+} channel [73] .

Store Operated Ca^{2+} Channel (SOCC)

SOCC causes the Ca^{2+} entry into the cell when ER Ca^{2+} decreases [74], yet a few detailed models are present on the underlying mechanism. Ong et al. [75] first tried to fit experimental data to SOCC model. The Model assume that the decrease of Ca^{2+} concentration in ER leads to the activation of SOCC and vice versa. However, the $[Ca^{2+}]$ in bulk ER does not effects the channel, instead model split the channel into two regions. One is under the membrane and other is the bulk ER. The $[Ca^{2+}]$ in ER sub-membrane region (denoted by c_e) affects the SOCC activation or inactivation. Another significant aspect of the model is the inclusion of a time dependent variable, h, via heuristic inactivation. The variable h is determined solely by fitting to the experimental data; it has no mechanistic base. The flow through the model is:

$$J_{soc} = f(c_e)h \qquad\qquad 2.26$$

$$\tau_h \frac{dh}{dt} = h_\infty(c) - h \qquad\qquad 2.27$$

The variables, f and h, are the decreasing functions. As there is no mechanistic explanation of these function, only their shapes matters.

The model of binding of STIM to Orai was constructed by Hoover and Lewis [76].
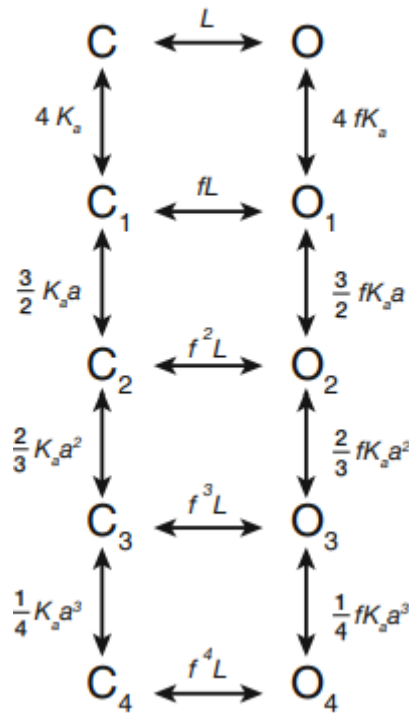
Figure 9. Model of Orai binding with STIM. *C* denote the close configuration of Orai and O denotes the Open configuration of Orai. Each configuration can bind upto 4 STIM molecule.

The Orai molecule, as shown in the Figure 9, can have up to ten states. In closed conformation of Orai C, STIM can bind at any four binding site, having equilibrium constant for each site is K_a. The equilibrium constant of transition from $C \leftrightarrow C_1$ is Ka. Similarly, the equilibrium constant for second STIM binding is aK_a, demonstrating the direct cooperativity of STIM binding with Orai. The value of *a* is either less than or greater than 1 shows the positive or negative cooperativity. A similar binding process exists for the open configuration of Orai, but the equilibrium constant is modified by a factor *f*. Hoover and Lewis calculated the values of the factors by fitting them to the experimental data. There model predict that STIM binds to Orai with negative cooperativity, but because of its binding at open configuration leading to the positive cooperativity due to the preferred open configuration.

Inositol Triphosphate Receptor (IP₃R) and Ryanodine Receptor (RyR)

IP₃R and RyR are the two most important channels observed in many cell types for Ca^{2+} oscillation and waves. The open probability of channels is affected by various factors such as IP_3, Ca^{2+}, ATP (an essential modulator of IP_3R), and there is also a substantial time dependency in ligand binding. There are different reviews available for IPR in the literature [77] [78]. IPR exists in homotetrameric form, a combination of four subunits, each of the same type. Dupont and Combettes constructed the model to study the effect of different subtypes' properties on oscillatory behavior [79]. The open probability P_o of IPR is an increasing function of $[Ca^{2+}]$ when $[IP_3]$ is fixed, that is, Po increases at low $[Ca^{2+}]$ and decreases at high $[Ca_{2+}]$. Similarly, at fixed $[Ca^{2+}]$, Po is an increasing function of $[IP_3]$. Studies show that the estimated value of Po is less than 0.1 [80] but in recent studies, it is estimated to be between 0.3 and 0.8 [81]. IPR has two Ca^{2+} binding site and one IP_3 binding site. One Ca^{2+} binding site is activating, while the other is inactivating. At low $[Ca^{2+}]$, slow release of Ca^{2+} from IPR initiates the positive feedback loop, increases the Po and cause increase in $[Ca^{2+}]$. This positive feedback loop is Calcium-Induced-Ca^{2+} Release (CICR).

The earliest model of IPR that incorporates the sequential activation ad inactivation of channel is given by De Young and Keizer [82] as shown in Figure 10.
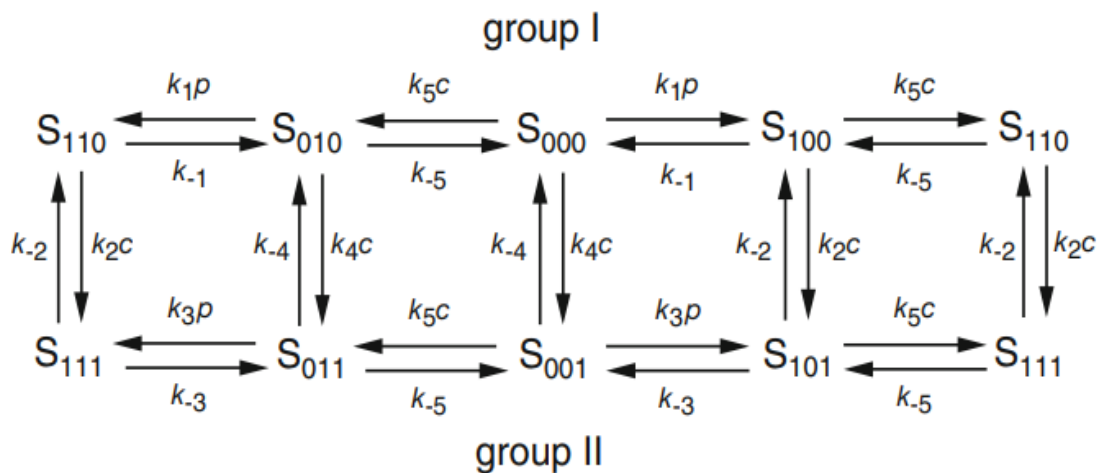
Figure 10. Schematic diagram of IPR model presented by De Young and Keizer. C shows $[Ca^{2+}]$ and p shows $[IP_3]$.

De Young and Keizer assumed that IPR consist of three independent subunits, one for activating calcium, one for inactivating Ca^{2+} and one for IP_3 binding. All of three subunits must in in active form of Ca^{2+} flux. Each subunit is labelled as S_{ijk} where i, j, and k can be either 1 or zero. One indicates binding site is occupied and zero shows the binding site is not occupied. i refers to IP_3 biding site, j for Ca^{2+} activating site and k shows Ca^{2+} inactivating site. The flux through channel starts only when three subunits (Ca^{2+} and IP^3) are in state S_{110} (one IP_3 and one activating Ca^{2+} is attached). The original article by De Young and Keizer is referred to for model parameters and equations.

The model of De Young and Keizer is simplified by Li and Rinzel [83]. Since the binding of IP_3 and Ca^{2+} at activating site is simultaneous, they infer that the receptor is in quasi-steady-state w.r.t IP_3 and Ca^{2+} ion. The model parameters and equations are present in the original paper of Li ad Rinzel [83].

RyR is involved in excitation-contraction coupling in heart and skeletal muscles, as well as in other cell types such as airway smooth muscles, neurons, exocrine acinar cells, oocytes. RyR behaves similarly to IPR in that it is triggered by high $[Ca^{2+}]$ and thus mediates CICR [84]. The simplest model for RyR was constructed by Friel to view the $[Ca^{2+}]$ oscillation in sympathetic neurons [85]. The Ca^{2+} flux in this model is an increasing function of $[Ca^{2+}]$.

The flux through the channel is:

$$J_{RyR} = \left(k_1 + \frac{V_r c^3}{K^3 + c^3} \right)(c_e - c) \qquad 2.28$$

The cytosolic and ER Ca^{2+} concentrations are represented by c and c_e, respectively. The first term in the equation denotes the channel's open probability, which increases as Ca^{2+} increases, and can be read as CICR. The second word is simply a force that drives Ca^{2+} flux through the channel.

Ca^{2+} Buffers

Almost in all the cells, Ca^{2+} is heavily buffered. Approximately 99% of the available Ca^{2+} binds with the binding proteins. Most prevalent Ca^{2+} buffers are calretinin, calsequestrin, calbindin and parvalbumin.

A simple chemical reaction for Ca^{2+} buffering is:

$$P + Ca^{2+} \overset{k_+}{\leftrightarrow} B \qquad \qquad 2.29$$

P a buffering molecule and B is a buffered molecule. The differential equations for Ca^{2+} bound to buffer and concentration of free Ca^{2+} is:

$$\frac{\partial c}{\partial t} = D_c \Delta^2 c + f(c) + k_- b - k_+ c\,(b_t - b) \qquad \qquad 2.30$$

$$\frac{\partial b}{\partial t} = D_b \Delta^2 b - k_- b + k_+ c\,(b_t - b) \qquad \qquad 2.31$$

Where, bt is the total buffer concentration, k_{-1} is the rate of Ca^{2+} release from buffer, k_{+1} is the rate of Ca^{2+} uptake by the buffer, f_c shows all other reaction involving free calcium. $D_c \Delta^2 c$ and $D_b \Delta^2 b$ model the diffusion of Ca^{2+} and buffer, having diffusion coefficient of D_c and D_b.

2.4 Mathematical Models for Ca^{2+} Signaling in Cancer

Sr. No	Objective	Model type	Parameters	Results	Ref.
1.	The objective of this study was to: 1. Understand the cytosolic Ca^{2+} oscillation applied in both electrically excitable and non-excitable cells. 2. The model has split into two parts: the minimal model and the extended model. The minimal model has two parameters out of six, whereas the expanded model has three or four parameters out of six.	Deterministic models containing ODEs.	The following parameters were included in the model: 1. Concentration of IP$_3$ 2. Concentration of cytosolic calcium 3. Concentration of ER calcium 4. Concentration of mitochondrial calcium 5. Ca^{2+} binding sites occupied by the buffer in the cytosol 6. Fraction of IPR in a sensitized state	Results include: 1. A self-sustaining oscillation exists if any of the variables has an activatory impact on itself, i.e., positive feedback caused by CICR, exhibited by IP$_3$R and RyR Ca^{2+} release channels. 2. By removing external calcium, the cessation of oscillation will occur in most cells like Hela cells. For most cells, external Ca^{2+} is not required like in salivary glands. 3. Oscillation amplitude along with frequency is necessary to explain the behavior of Ca^{2+} signaling in the cells.	[86]

| 2. | To develop an integrative model for Ca^{2+} signaling and metabolism in mitochondria in non-excitable cells. Their objective is to study the:

1. Trajectory analysis of the relationship of Ca^{2+} changes in the cytosol, ER, and mitochondria.

2. The impact of changes in cytosolic Ca^{2+} on mitochondrial metabolites.

3. The effect of Ca^{2+} variation on cytosolic/mitochondrial Ca^{2+} exchanges and mitochondrial metabolism. | Deterministic model, consist of ODEs. | The model parameters consist of seven ODEs and 4 conservation equations,

1. Cytosol Ca^{2+} concentration
2. Mitochondrial Ca^{2+} concentration
3. Fraction of inactivated IP_3R
4. Mitochondrial NADH concentration
5. Mitochondrial ADP concentration
6. Cytosolic ADP concentration
7. Voltage difference across the inner mitochondrial membrane

Conservation equations
1. Conservation of total NADH
2. Conservation of ADP/ATP in mitochondria
3. Conservation of ADP/ATP in cytosol | 1. Ca^{2+} release from mitochondria raises $[Ca^{2+}]$ in the cytosol, which activates the IP_3R, resulting in Ca^{2+} release from the ER.

2. Cytosolic Ca^{2+} achieves its maximum value just before ER Ca^{2+} reaches its minimum value.

3. The concentration of Ca^{2+} in mitochondria only rises during the rising period of the cytosolic Ca^{2+} peak. $[Ca^{2+}]$ in mitochondria does not return to baseline.

4. Complete inhibition of NCX activity reduces the frequency of Ca^{2+} spikes, which occurs due to slower Ca^{2+} release from mitochondria and thus delayed priming of the IP_3R to produce the cytosolic Ca^{2+} spike.

5. Changing the rate constant of the MCU forecasts a biphasic effect: increasing the activity of the MCU | [87] |

first increases, then reduces the frequency of oscillations.

6. When both NCX and MCU are inactive, their model includes a reversible flux whose direction is determined by the electrochemical gradient. The possible candidate is mPTP. According to the model results, its reduction reduces the frequency of Ca^{2+} oscillation.

7. Cytosolic Ca^{2+} spikes result in a huge and long-lasting increase in NADH, which stimulates the Krebs cycle and raises mitochondrial potential. However, Ca^{2+} entry from the cytosol to the mitochondria reduces the voltage difference across the mitochondrial membrane. The biphasic voltage shifts causes ATP synthesis.

3.	Their objectives were to study the: 1. Different cells with varying periods of Ca^{2+} oscillations have a common dynamical structure. 2. To suggest a testable mechanism for how cells produce oscillations based on their dynamic structure.	Deterministic model consisting of ODEs	The following parameters were present in the respective study: 1. Concentration of Ca^{2+} in the cytosol 2. Concentration of Ca^{2+} in ER 3. IP_3 Concentration 4. Variable that controls the rate of activation and inactivation by calcium The following fluxes were present: 1. Ca^{2+} flux through SERCA 2. Flux Through plasma membrane 3. Efflux through PMCA	The Model predicted the following results: 1. By increasing the Ca^{2+} flux or concentration of IP_3, the oscillation frequency increases. 2. Ca^{2+} influx influences oscillation frequency but is not required for oscillations to exist.	[88]
4.	Build a mathematical model to study the: 1. HYS cells, a cell line of the human parotid, when stimulated with ATP and carbachol (CCh), exhibit the	Deterministic mathematical model of ODEs	The Model contains three main compartments: 1. The Region inside ER, Region near IPR (small micro-domain), and the cytosol The following fluxes were included in the model:	The model results showed that: 1. When the external Ca^{2+} flux is removed, the oscillation frequency steadily decreases until it stops. 2. Although IP_3 oscillation is not required to cause Ca^{2+} oscillation	[89]

	coupled Ca^{2+} oscillation preceding IP_3 spike peaks.		1. The flux through IPR 2. The flux from the microdomain to the cytosol 3. Some leak flux across the ER membrane 4. The re-uptake flux through SERCA pump. 5. Influx through the membrane via ROCC and SOCC 6. Ca^{2+} efflux through PMCA	in HSY cells, a transient increase in Ca^{2+} frequency was observed due to the photolysis of caged IP_3. 3. When calcium-induced PLC activation was blocked, the amplitude and frequency of the oscillation decreased.	
5.	Their Objective was to: 1. Understand the impact of MAMs (mitochondria-associated-membrane) Ca^{2+} dynamic on cell Ca^{2+} activities. 2. To validate the experimental findings of MAMs and obesity in mouse liver cells, as well as obesity-related	Deterministic model consisting of ODEs	The model was divided into two sub-models: Model for intracellular Ca^{2+} dynamic, consist of following parameters: 1. Total intracellular Ca^{2+} concentration 2. ER Ca^{2+} concentration 3. Ca^{2+} concentration in MAM 4. Ca^{2+} concentration in mitochondria	The model results showed that: 1. At lower Ca^{2+} concentrations, as the stimulus dosage rises, the liver of obese mice reaches saturated cytosolic Ca^{2+} concentrations faster than the cells from healthy mice. 2. The model reproduces the experimental finding that hepatocytes with higher MAM show an ATP-induced Ca^{2+} transient with higher peaks in	[89]

	cellular changes that are closely linked to Ca^{2+} signaling.		5. Concentration of IP_3 in cytosol and MAM 6. Activation variables of IPRs in cytosol and MAM Model for mitochondria metabolic pathways and membrane potential, consist of following parameters and fluxes: 1. Concentration of ADP in mitochondria and cytosol 2. Concentration of NADH in mitochondria 3. Voltage difference across the inner mitochondrial membrane	mitochondria, whereas hepatocytes from obese animals generate higher mitochondria Ca^{2+} peaks than hepatocytes from lean animals. 3. Obese mice have greater levels of IPR and MCU, as well as higher levels of MAMs, so they exhibit quicker Ca^{2+} oscillation.	
6.	The objective of this study was to: 1. Recognize the spatiotemporal dependency of Ca^{2+} and IP_3 in cardiac myocytes. 2. Determine the set of parameters that govern	Partial differential equations solved with finite element method.	The parameters studied were: 1. Concentration of Ca^{2+} in cytosol. 2. Concentration of IP_3 in the cytosol. The spatial effects of the parameters are also considered, x is the position variable, distance from	The model result showed: 1. The relationship between Ca^{2+} and IP_3 is nonlinear in cardiac myocytes. 2. IP_3 diffuses to the cytosol from the membrane, binds to IP_3R, opens the channel, and releases calcium; Ca^{2+} binds to PKC, which is	[90]

	the Ca^{2+} concentration in the cytosol.		the Ca^{2+} source and t is the time variable. The model contains the following fluxes: 1. Flux for IP$_3$ receptor 2. Flux for Leak 3. Flux for SERCA pump 4. Flux for IP$_3$ production 5. Flux for kinase and phosphorylation	triggered by DAG; activated PKC regulates cellular processes. Shows that Ca^{2+} and IP$_3$ concentrations are interdependent and that Ca^{2+} and IP$_3$ concentrations in cells are needed for cardiac myocytes. 3. Source channels, including leaks and pumps, work in concert to maintain Ca^{2+} and IP$_3$ concentration at optimal levels for the initiation and termination of different processes in cardiac myocytes.	
7.	Objective of this study was to: 1. Build a mathematical model to demonstrate the effect of Ca^{2+} concentration in Alzheimer's disease.	Three dimensional mathematical equation consisting of ODEs solved by finite element technique.	Following parameter were discussed in this paper: 1. Ca^{2+} dynamic in the presence of buffer 2. VGCC mediated Ca^{2+} dynamic 3. NCXL mediated Ca^{2+} dynamic 4. Ca^{2+} dynamic in ER and mitochondria	Model results showed that: 1. The two major Ca^{2+} influx channels involved in Alzheimer's disease are VGCC and NCLX. 2. Any change in VGCC and NCLX causes an increase in cytosolic Ca^{2+} concentration; similarly, a reduction in buffer and defects in	[91]

				ER and Mitochondria cause an increase in cytosolic Ca^{2+} concentration. 3. The addition of exogenous buffers such as EGTA and BAPTA regulates the increased Ca^{2+} fluctuation.	
8.	They use mathematical modeling and live-cell intracellular measurement to: 1. investigate Ca^{2+} signaling dysregulation in KYSE-150, a human esophageal squamous cell cancer cell line. 2. Determine whether the combination of afatinib (an FDA-approved treatment for esophageal cancer) and RP4010 (a SOCC	Deterministic model consisting of ODEs	The parameters discussed for model building include: 1. Ca^{2+} concentration in the cytosol. 2. Ca^{2+} concentration in ER 3. Concentration of IP_3. 4. Rate at which Ca^{2+} activates IP_3R. The following fluxes were included: 1. Flux of Ca^{2+} from ER through IP_3R channel 2. Flux of Ca^{2+} from cytosol to ER through SERCA pump	1. The mathematical and experimental results indicate that both drugs reduce the frequency of Ca^{2+} oscillations synergistically and have a significant impact on cell viability in an esophageal cell line. 2. 2. Afatinib, a TRI, inhibits the P13K/Akt and MEK/ERK signaling pathways, while RP4010 inhibits intracellular Ca^{2+} oscillation in a dose-dependent fashion.	[92]

	blocker) is helpful for the treatment. 3. Determine the optimal concentration of both drugs for combined treatment.		3. Flux through leaks includes entry via unspecified channel plus SOCC mediated Ca^{2+} entry 4. The flux through plasma membrane pump.		

2.5 Mathematical Models for NB

9.	The objective of this study was to: 1. Create a mathematical model to determine an optimal chemotherapeutic schedule that minimizes toxicity while maximizing effectiveness.	ODE model for pharmacodynamics and pharmacokinetic of Topotecan	There are four mathematical models discussed in this paper, 1. Topotecan plasma pharmacokinetics, include following parameters: Clearance, volume of the central compartment, and inter-compartmental parameters. 2. Tumor growth include following parameters:	The model Results showed that: 1. Protracted schedule of topotecan to obtain systematic exposure between 80 and 120 ng/mL h/dose in high-risk NB patients is highly effective. 2. Increasing the duration of therapy was essential and resulted in a higher response rate.	9.	[93]

	2. Determine the cytotoxic impact of Topotecan, a topoisomerase inhibitor, on tumor tissue as well as the hematopoietic system. 3. Compare different topotecan systematic exposure and schedule of treatments.		Tumor proliferating cells, and tumor Quiescent cells. 3. Neutrophil dynamic, include following parameters: Topotecan plasma concentration, concentration of different proliferating cells, concentration of non-proliferating cells, and concentration of circulating neutrophils. 4. Platelet dynamic include similar parameter sets as that of neutrophil dynamic.		
10.	Their objective was to: 1. Study the role of VEGF in tumor growth and progression in IMR-32.	Compartmental mathematical model, consisting of ODEs	The model contains 10 quantities: 1. Rate of change of cells in the G1 phase 2. Rate of change in the S phase 3. Rate of change in the G2 phase	The Model results showed that: 1. Bevacizumab concentration is inversely linked to tumor growth and VEGF level. 2. Bevacizumab has no impact on tumor suppression when administered in a single large	[94]

	2. Study the effect of bevacizumab (Avastin; a humanized anti-VEGF-A antibody), the first angiogenesis inhibitor, against NB.		4. Rate of change in Q(quiescent) phase 5. Rate of change in the N (necrosis) phase 6. VEGF signaling (R) 7. Concentration of TNF-α (A) 8. Vasculature (V) 9. Drug kinetics of Bevacizumab (E, X)	dose or in smaller doses on a regular basis.	
11.	Their objective was to: 1. Create a mathematical model that describes the connection between immune cells, cancer cells, and viral cells in paediatric NB patients. 2. Create a Mathematical model both for continuous and periodic therapy	Non-linear ordinary differential equations	The following parameters were considered in this model: 1. NB tumor cells 2. Tumor suppressor cells: are the immune cells that suppress the action of tumor cells 3. Immune suppressor cells: are immune cells that suppress the activation or proliferation of tumor suppressor cells. 4. Oncolytic Virus : Celyvir, the therapy used.	1. Stability and bifurcation analysis are used to determine whether treatment induces tumor free equilibrium or tumor progression. 2. The model shows the existence of a viral load threshold value that could ensure the patient's recovery. 3. The model insists that both the duration of treatment and the intensity of the viral load must be adequate to guarantee the	[95]

			therapy's success. Failure to provide appropriate treatment may result in viral recurrence. 4. The combination of Celyvir and other chemotherapies may be helpful for tumor eradication.	

2.6   Cell Cycle Phases Model

Carcinogenesis may result in the loss of control over cell cycle leading to the abnormal cell population. Cell cycle can be used as an object for the treatment against cancer. Different control models for the cell cycle are formulated for analysis and optimization of different protocols of drug administration [96] [97]. Cell cycle is the sequence of phases that are repeated by each cell from its birth to division. It consists of G1 (growth phase), S (synthesis phase), G2 and M phases (division phase). After division two progeny reenter the G1. It might possible that either one of both the progeny becomes dormant and enters the G0 phase and after some or long duration it might re-enter the G1 phase [98]. There is multiple regulatory mechanism that controls the progression of cells from each phase. Any disturbance in these mechanism may lead to the error that propagates through the signaling networks and leads to the cancer development [99].

The effect of drug either as a killing agent or blocking agent can be considered by introducing the control variables. In compartmental model, the application of killing and blocking agents is equals to the death of a fraction of cells in the flow between compartments. For example, if f_a denotes the drug action, only a fraction (1- f_a(t)) of the outflow from the compartment contains live cells ($0 \leq f_a \leq 1$).

2.7   Research Gap

Based on a comprehensive literature review, it has been observed that there is a lack of studies utilizing mathematical modeling to examine the influence of Ca^{2+} signaling on NB cells. To address this research gap, our intention is to utilize preexisting mathematical models for Ca^{2+} signaling to gain insights into the dynamics of NB. We aim to assess the impact of the rate of Ca^{2+} intake on cell growth and explore the effects of various chemotherapeutic agents and Ca^{2+} regulators on NB growth and inhibition. By employing this approach, we seek to provide a deeper understanding of the role of Ca^{2+} signaling in NB and propose potential therapeutic interventions that target this signaling pathways

<div align="right">**Chapter 3**</div>

3 Methodology

Our study extended the work conducted by Wacquier *et al.*[100], which focused on investigating the role of $[Ca^{2+}]i$ in three cellular compartments: cytosol, endoplasmic reticulum (ER), and mitochondria. Additionally, we have incorporated modifications to the model presented in Wallace *et al.*'s study [101] in order to simulate the impact of various chemotherapeutic agents and Ca^{2+} regulators on cell growth. The model developed by Wacquier *et al.* for Ca^{2+} signaling is rooted in prior experimental studies and incorporates kinetic expressions of various channels and pumps. They adjusted multiple parameters to assess intracellular Ca^{2+} expression in three compartments, using HeLa cells as a reference. Likewise, Wallace *et al.* focused on studying the cell cycle dynamics of both monolayer and spheroid models of a NB cell line. They utilized data from monolayer treatment of SK-N-SH NB cells with 15-deoxy-PGJ$_2$ and expanded it by incorporating growth rate data from untreated SK-N-SH NB spheroids. These two studies serve as the basis for the development of a comprehensive model that integrates Ca^{2+} signaling into the process of cell growth and assesses its combined influence with different chemotherapeutics. Likewise, to depict the effect of chemotherapy on cell death or apoptosis, a pharmacodynamics term is introduced in the cell cycle phases model. In pharmacodynamics, the effect of drug concentration on cell growth and apoptosis is checked. MATLAB, specifically the ode15s solver, is employed to execute all the necessary computations.
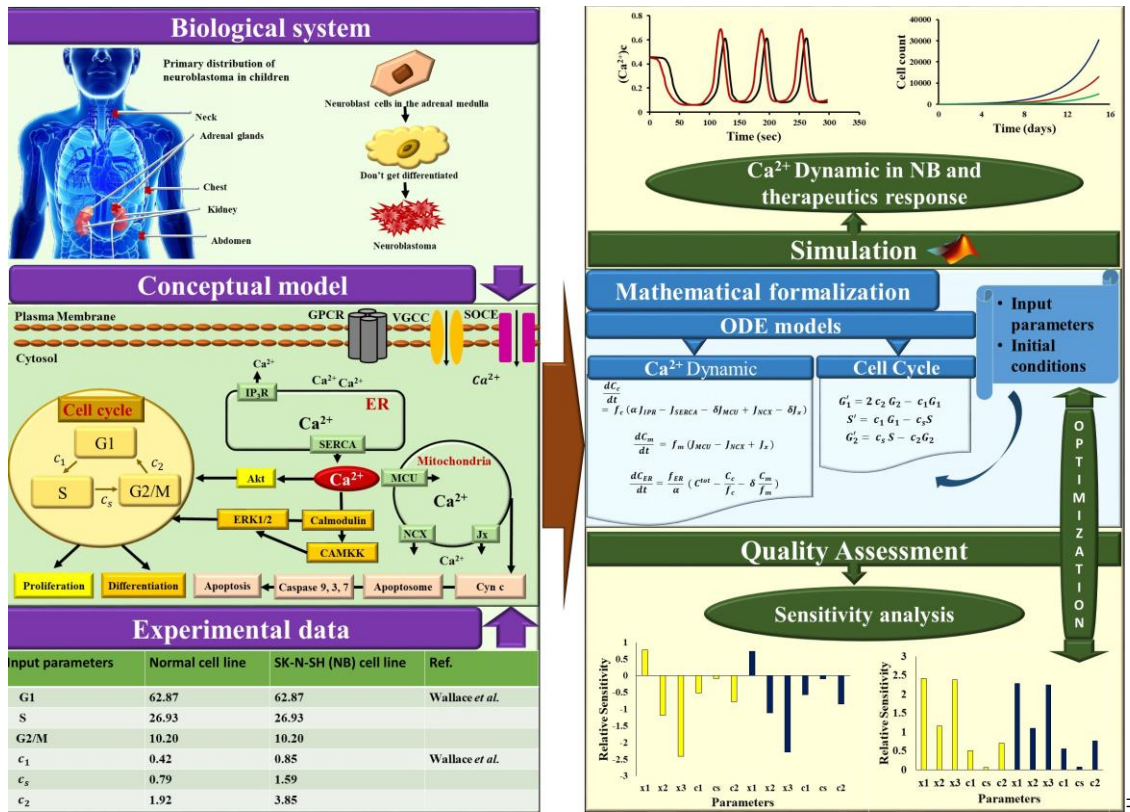
Figure 11: Diagrammatic illustration of the methodology followed for this study. A conceptual model representing the metabolic pathways involving NB dynamics was constructed. The extracted experimental data of NB-specific *in vitro* and *in vivo* studies was subjected to the ODEs, representing the mathematical formulation of a conceptual model. The model was simulated under different conditions to analyze the NB growth dynamics along with different therapeutics. The local sensitivity analysis revealed the relative sensitivity of model parameters, which helps in parameter extraction and optimization. Parameter Extraction and Optimization

The model parameters of Wacquier *et al.* are optimized to mimic the simulated Ca^{2+} dynamics observed in normal and cancerous cells. Two key parameters, namely, the total Ca^{2+} concentration (C_t) and the fraction of free over buffer bound Ca^{2+} in the cytosol, mitochondria, and ER (f_c), are optimized based on the researchers' best understanding to produce the oscillation pattern of normal and tumorigenic condition like observe in Stewart *et al.'s* study. Additionally, the parameters related to cell cycle dynamics such as the Ca^{2+} concentration in G1, S, and G2/M phases are also optimized to replicate the observed behavior [102]. During the simulations, it is assumed that in tumorigenic conditions the concentration of Ca^{2+} is doubled and the rate of transitions between phases is also doubled compared to normal cells, parameter values are reflected in Table 2.

Additionally, local sensitivity analysis of different parameters is performed to assess the relative significance of each parameter in predicting cell growth, detailed explanation is provided in Appendix A.

Table 2

Summary of cell growth model parameters and initial conditions. The parameter values extracted from the SK-N-SH monolayer culture [101].

Cell line	Normal cell line	SK-N-SH
Source material	Wallace *et al.* [101]	Wallace *et al.* [101]
Observed G1	62.87	62.87
Observed S	26.93	26.93
Observed G2/M	10.20	10.20
Transition rates	Optimized values	Wallace *et al.* [101]
c_1	0.42	0.85
c_s	0.79	1.59
c_2	1.92	3.85
Cytosolic Ca^{2+} concentration	Pande *et al.* [102]	Optimized values
x_1	0.75	1.51
x_2	0.72	1.44
x_3	0.74	1.49
C_t	1000	1200
f_c	0.01	0.02

3.1 Model Building

A mathematical model for Ca^{2+} dynamics is built in MATLAB with the help of built in ODEs. The optimized Wacquier *et al.* model of Ca^{2+} signaling consists of seven ODEs, four conservation equations, and eleven chemical equations for fluxes. The ODEs include cytosolic Ca^{2+} concentration, inactivated IP$_3$ receptor, mitochondrial Ca^{2+} concentration, mitochondrial NADH concentration, mitochondrial ADP concentration, cytosolic ADP concentration, Voltage difference across inner mitochondrial membrane, and ER Ca^{2+} concentration. Similarly, chemical

equations for the fluxes include: Ca^{2+} flux through IP$_3$, Ca^{2+} flux through unidirectional SERCA ATPase pump, flux from cytosol to mitochondria through MCU, rate of Ca^{2+} extrusion out of mitochondria through NCX, bidirectional Ca^{2+} leaks between cytosol and mitochondria (J$_x$), rate of NADH production by pyruvate dehydrogenase (PDH), rate of NADH production induce by the MAS NADH shuttle (AGC), rate of NADH oxidation (J$_0$), rate of ATP/ADP translocator (ANT), rate of ATP synthesis by F$_I$F$_O$-ATPase (F$_I$F$_O$), rate of ATP consumption by cytosol (HYD), and Ohmic mitochondrial proton leak (J$_{H, leak}$).

3.2 Model Equations

Following are the ODEs for Ca^{2+} signaling in three compartments including cytosol, ER, and mitochondria.

1. Cytosolic Ca^{2+} concentration

$$\frac{dC_c}{dt} = f_c \left(\alpha J_{IPR} - J_{SERCA} - \delta J_{MCU} + J_{NCX} - \delta J_x \right) \tag{1}$$

2. Fraction of inactivated IP$_3$ receptor

$$\frac{dR_i}{dt} = k_+ C_c^{n_i} \frac{1 - R_i}{1 + (\frac{C_c}{K_a})^{n_a}} - k_- R_i \tag{2}$$

The equation shows the regulation of Ca^{2+} oscillation due to IP$_3$ and Ca^{2+}.

3. Mitochondrial Ca^{2+} concentration

$$\frac{dC_m}{dt} = f_m \left(J_{MCU} - J_{NCX} + J_x \right) \tag{3}$$

4. Cytosolic ADP concentration

$$\frac{d[ADP]_c}{dt} = J_{HYD} - \delta J_{ANT} \tag{4}$$

5. Mitochondrial ADP concentration

$$\frac{d[ADP]_m}{dt} = J_{ANT} - J_{FIFO} \tag{5}$$

6. Voltage difference across inner mitochondrial membrane

$$\frac{d\Delta\psi}{dt} = \frac{a_1 . J_o - a_2 . J_{FIFO} - J_{ANT} - J_{H,leak} - J_{NCX} - 2. J_{MCU} - 2. J_x - J_{AGC}}{C_p} \quad (6)$$

C_p include both membrane capacitance and faraday's constant.

7. ER Ca^{2+} concentration

$$\frac{dC_{ER}}{dt} = \frac{f_{ER}}{\alpha} \left(C^{tot} - \frac{C_c}{f_c} - \delta \frac{C_m}{f_m} \right) \quad (7)$$

For the comprehensive information regarding conservation equations, fluxes, and detailed terminology, it is recommended to consult the original paper of Wacquier *et al* [100]. Likewise, the mathematical model of cell cycle phases is built in MATLAB. It consists of three phases, G1 phase, S phase, and G2/M phase. In this study, we extend the work done by Wallace et al. [101],
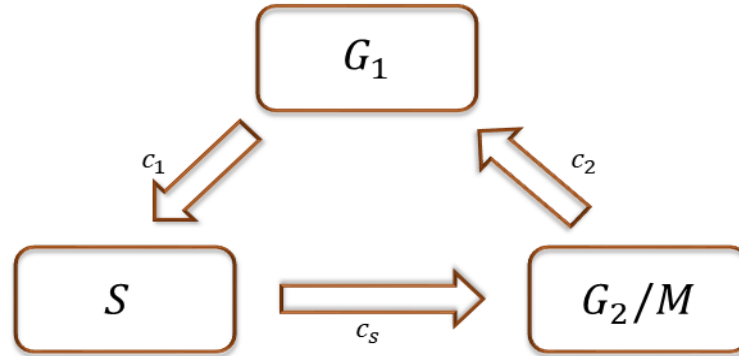
Figure 12: Flow diagram representing general model of cell cycle without G$_0$ phase.

The overview of general cell cycle phases is representing in Figure 12, G1 shows the average number of cells in G1 phase and c_1 is the transition rate of the cells from G1 phase to S phase. Likewise, S and G2/M denotes the initial number of cells in the respective phases and c_s and c_2 are the transition rate in the respective cell cycle phases. Each cell cycle phase is represented as a separate compartment. Usually, G2 and M phases are combined as one compartment. If G$_0$ phase is not considered, then according to the exponentiality assumption, the number of cells in different cell cycle compartment is represented by a system of ODEs.

$$G_1' = 2\,c_2\,G_2 - c_1 G_1 \tag{8}$$

$$S' = c_1\,G_1 - c_s S \tag{9}$$

$$G_2' = c_s\,S - c_2 G_2 \tag{10}$$

The model equation can incorporate the effect of drugs, either as cytotoxic agents or blocking agents, as control variables to represent the chemotherapeutic effect. In a compartmental model, the application of cytotoxic and blocking agents can be represented as the death of a fraction of cells in the flow between compartments. This allows for the simulation of the impact of these agents on the overall dynamics of the system. For example, if f_a denotes the drug action, only a fraction (1- f_a(t)) of the outflow from the compartment contains live cells ($0 \leq f_a \leq 1$) [97].

To describe the effect of a drug on cells, a saturation equation without cooperativity is employed. This mathematical equation delineates the relationship between the concentration of the drug and the fraction of cells in arrest. One commonly used saturation equation is modeled by the Michaelis-Menten equation, (Equation 11).

$$f_a = \frac{C}{K_a + C} \tag{11}$$

C denotes the drug concentration and parameter K_a is the concentration effect (IC$_{50}$ or EC$_{50}$) of drug. For example, consider the effect of drug on G2/M phase, the ODEs for this case will be:

$$G_1' = 2\,(1 - f_a(t))\,c_2\,G_2 - c_1 G_1 \tag{12}$$

$$S' = c_1\,G_1 - c_s S \tag{13}$$

$$G_2' = c_s\,S - c_2\,(1 - f_a(t))\,G_2 \tag{14}$$

$f_a(t)$ =0 represents no action of drug and $f_a(t)$=1, represents maximum action of drug.

One limitation of this model is its failure to incorporate the quiescent phase, which is crucial in real-life scenarios. When cells are exposed to drugs, they may survive but lose their ability to proliferate or experience delayed proliferation. This aspect adds complexity to the process of parameter estimation, making it more challenging. This limitation can be particularly problematic in certain cancer types such as breast and ovarian cancer [103] [104] and leukemia [105]. In leukemia cases, cells remain in a quiescent state and are not affected by cytotoxic agents.

Thus, neglecting the insensitivity of dormant cells to anticancer drugs can lead to significant issues. Despite of these limitation, the ODEs presented here for the compartmental cellular growth model accurately describe the quantitative behavior of cellular growth of SK-N-SH observed in Wallace *et al.* [101]'s study of monolayer SK-N-SH cells.

3.3 Trajectory Analysis

The trajectories of Ca^{2+} signaling model are analyzed to understand the Ca^{2+} oscillation pattern in three compartments: cytosol, ER, and mitochondria in both normal and the diseased conditions. Likewise, the qualitative pattern of cell growth is also analyzed by the trajectories of cell growth model in the presence and absence of therapies. This analysis provides valuable insights into the efficacy and potential synergistic effects of the drugs in inhibiting NB cell growth.

<div align="right">**Chapter 4**</div>

4   Results and Discussion

In non-excitable cells, the Ca^{2+} oscillations are supposed to be regulated by the different Ca^{2+} channels or pumps notably by the internal stores IP_3R and SERCA. The opening of IP_3R generate Ca^{2+} oscillations or repeated spikes. The respiratory chain reaction in mitochondria generate the negative potential across the inner membrane, creating a charge difference (known as membrane potential ($\Delta\psi$)) that allows the MCU to transport Ca^{2+} into mitochondria, which causes the depolarization of mitochondrial membrane and reduce the driving force for further Ca^{2+} entry. The mathematical model of Ca^{2+} signaling produces an oscillatory pattern of Ca^{2+} in cytosol, ER, and mitochondria with initial concentration of 0.45, 107.71, and 0.29 (units in µM) respectively, shown in Figure 13. When the cytosolic Ca^{2+} returns to its basal level, mitochondria release Ca^{2+} through NCX or Ca^{2+} proton exchanger. Initially, Ca^{2+} increases slowly both in cytosol and in ER, while Ca^{2+} in mitochondria decreases. When cytosolic Ca^{2+} reaches its peak, it stimulates the IP_3Rs and ER Ca^{2+} starts to decrease. The Ca^{2+} in mitochondria starts to increase only during the first rising phase of cytosolic Ca^{2+}. When ER Ca^{2+} reaches its minimum value, cytosolic Ca^{2+} reaches its maximum value. During the period of high cytosolic Ca^{2+}, ER starts to refill. The slop began to change when the rate of ER Ca^{2+} increase is imposed by the rate of Ca^{2+} release form mitochondria. As long as mitochondrial Ca^{2+} is concerned, it keeps accumulating when the cytosolic Ca^{2+} reaches its peak value. The Ca^{2+} in mitochondria finally decreases until the onset of second cytosolic Ca^{2+} peak, but it does not return to its basal level during the inter-spike interval. The ODEs for Ca^{2+} signaling model is present in methodology section from equations 1 to 7 and the detailed oscillatory pattern is shown in Figure 13. The model equations, fluxes and parameters values are discussed in detail in Wacquier *et al.*'s study [106].
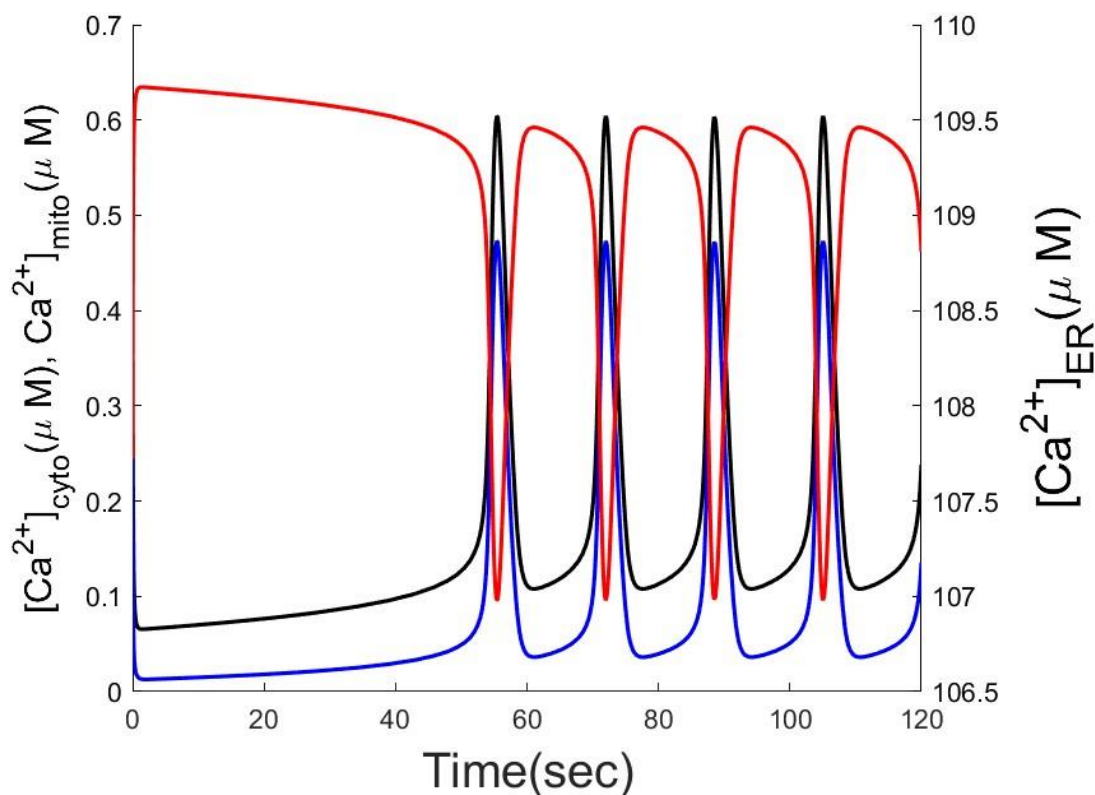
Figure 13: Ca^{2+} oscillation between cytosol, mitochondrial and ER. Curve in black shows the simulated waves of Ca^{2+} oscillation in cytosol, red shows the Ca^{2+} oscillation in ER, and blue shows the Ca^{2+} oscillation in mitochondrial. The image shows the sustained oscillation of by constant supply of $IP_3 = 1$ μM.

The tumorigenic cells exhibit characteristics pattern of Ca^{2+} signaling compared to the normal cells. Baldi *et al.* [107] studied the effect of SOCE in tumorigenic SKBR3 (luminal human epidermal growth factor receptor 2 positive cell line) and HBL100 (normal breast epithelial) cell line. The Ca^{2+} influx from SOCE due to Tg mediated ER depletion differed in both cell lines. The peak amplitude and initial rate of Ca^{2+} influx is same in both cell lines but the return of Ca^{2+} oscillation to the baseline Ca^{2+} in tumorigenic cell was more sustained and lowered as compared to the normal cell line. In a separate study, it was demonstrated that cultured human primary malignant glioblastoma multiforme cells exhibited a two-fold increase in the amplitude of SOCE compared to non-malignant human primary astrocyte control cells [108]. Similarly, store depletion causes the increased influx due to SOCE showed higher intracellular Ca^{2+} peak amplitude, and corresponding to increased Orai 1 protein expression showed in four metastatic melanoma cell

lines compared to the control melanocyte cell lines [109]. Similarly, KYSE-150, esophageal squamous cell carcinoma derived cell line studied by Zghu *et al.*, identified the altered expression of SOCE relative to the HET-100, a non-tumorigenic esophageal epithelial cell line [110]. The difference in global Ca^{2+} signaling using live cell imaging in the absence of stimulus showed that the esophageal squamous cell carcinoma cells showed a higher degree of spontaneous intracellular Ca^{2+} oscillations when compared to the normal cells.

We optimized C_t and f_c of the mathematical model for Ca^{2+} signaling to generate similar oscillation patterns in both normal and tumorigenic condition as observed in literature. The model was simulated for a duration of 120 seconds, allowing a comparison of oscillations behavior in normal and tumorigenic scenarios. The simulation results are presented in Figure 14, demonstrated distinct behaviors of $(Ca^{2+})i$ oscillations between normal (depicted by the red curve) and tumorigenic (represented by the black curve) conditions. In normal conditions, the frequency and amplitude of Ca^{2+} oscillations were tightly regulated, ensuring controlled cellular growth. Conversely, tumorigenic cells displayed abnormal Ca^{2+} oscillations with increased amplitude, leading to irregular cellular behavior and uncontrolled proliferation. The graphical outputs of simulated results revealed that tumorigenic cells manifest two oscillations per minute, whereas normal cells exhibit a reduced frequency of one and a half oscillations per minute. Furthermore, the predicted oscillation amplitude in normal cells measured 0.44, while tumorigenic cells demonstrated an increased amplitude of 0.50. The predicted behavior of Ca^{2+} signaling aligns with the findings presented by Teneale *et al.*'s study [111].
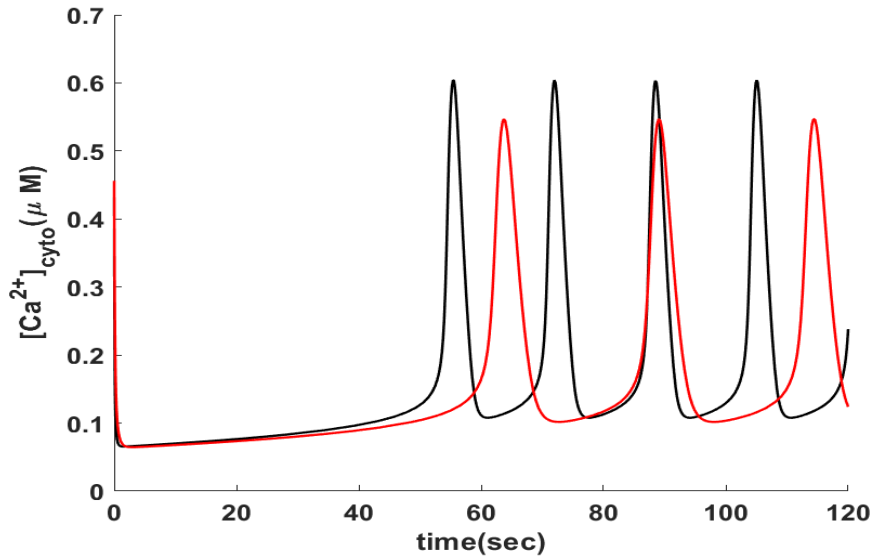
Figure 14: Simulated results of Ca^{2+} homeostasis in tumorigenic (black) and non-tumorigenic (red) cells. These changes occur due to the release from internal stores via IP_3 or $[Ca^{2+}]$, contributing to the excessive cell proliferation in NB (SK-N-SH). The simulated behavior is in agreement with the observations provided in [111].

To assess the effect of Ca^{2+} signaling on SK-N-SH cells, ($[Ca^{2+}]_c$) from Ca^{2+} signaling model was added to a mathematical model of cellular growth with the parameter values derived from the study of Wallace *et al.* [101]. The parameter values and initial condition for cell growth in normal and tumorigenic cells are given in Table 2. The parameters x_1, x_2, x_3 shows the phase specific Ca^{2+} concentration. These parameters were taken from the study of Pande *et al.* [102], they conducted an experiment on viable rat fibroblast to check the intracellular level of free $(Ca^{2+})_c$ in the G1, S, and G2/M cell cycle phases using flow cytometry. The graphical results of the mathematical model of cellular growth incorporating the effect of tumorigenic and non-tumorigenic ($[Ca^{2+}]_c$) on cell count is shown in Figure 15. The viable cells will be the sum of all cell cycle phases i.e, $viable\_cell\ (V_t)\ =\ G1_t + S_t + G2/M_t$. On day 1 the cell counts in G1, S, and G2/M phases are 62.87, 26.93, and 10.20 both in normal and tumorigenic condition, respectively. The simulation duration is 15 days and after 15 days both the normal and tumorigenic cell showed exponential growth. After simulation duration, the predicted cell count in normal

condition is 1912.77 while in tumorigenic condition, it is 34,324.81, showed that tumorigenic cells exhibit uncontrolled division, results are presented in Table 3. The unit of cell counts in cellular growth model is 10^6 μm^3.

Table 3

A comparison of cell count between tumorigenic and non-tumorigenic cell lines (parameters values were chosen from a neuroblatoma SK-N-SH cell line [101]) after 15 days.

Sr. no	Non-tumorigenic cell count	Tumorigenic cell count
1	1912.77	34324.81
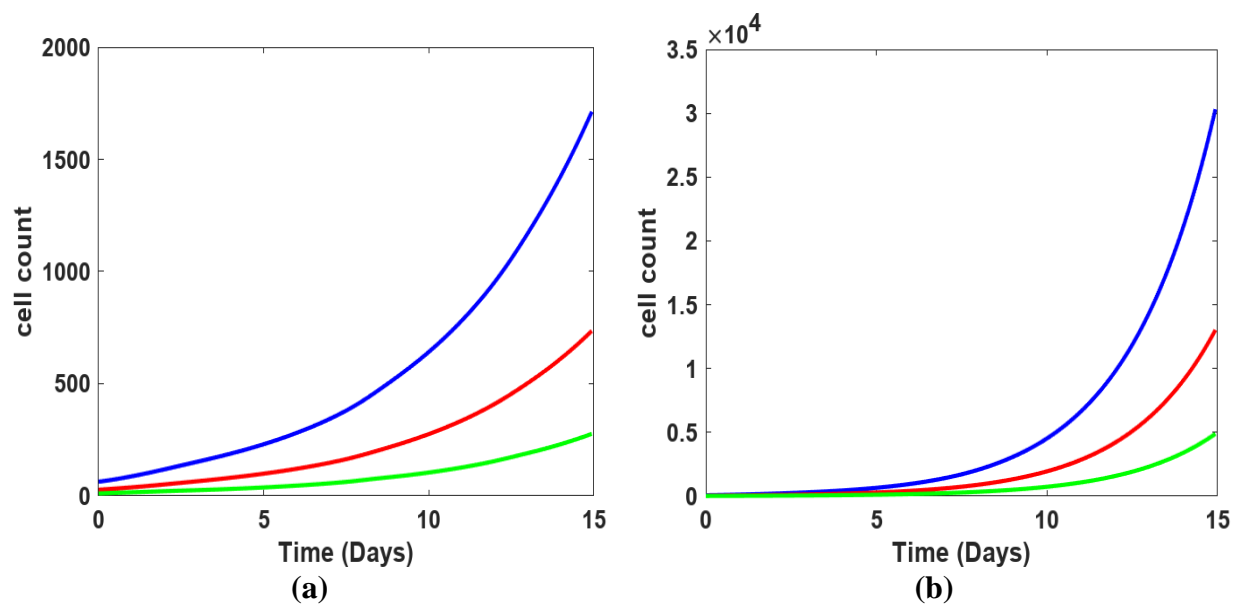
Figure 15: Simulated results of mathematical model of cell growth incorporating the effect of non-tumorigenic and tumorigenic $[Ca^{2+}]i$ in normal (a) and in SK-N-SH cell count (b). Blue curve shows the G1 phase, red curve shows the S phase, and green curve shows the G2/M phase.

After simulating cell growth in normal and tumorigenic cells, we incorporated the behavior of cancer therapeutics to examine their impact on cell growth and to identify optimal treatment schedules. The response data for the drugs were obtained from the study of Fulda *et al*. [112]. They conducted an *in-vitro* analyses of different cancer drugs and checked the cytotoxic activities of these drugs against six NB cell lines using monolayer proliferation assay. They identified the most effective and least effective drugs based on their ED$_{50}$ (*in-vitro* drug concentration for 50% growth

inhibition) values and drug's plasma level concentration, provided in Table 4. These drugs also possess anti-therapeutic activity against other cancer as well, detail of each drug's cytotoxic activity is provided in Table 4. Since these drugs have already demonstrated effectiveness against NB cells, we further studied their behavior using our methodology.

Table 4

Mean ED_{50} values and mean plasma level of drug concentration effective against six NB cell lines named as: IMR-5, Kelly, CHP-134, GI-CA-N, CHP-100, and SK-N-SH [112]. More effective drugs have ED_{50} values less than human plasma level while less effective values have ED_{50} values $\geq$ to human plasma level.

Sr. no	Drugs	Mean ED_{50} (nmol/ml)	Mean Plasma level (nmol/ml)
1	Mitoxantrone	0.06	1.655
2	Bleomycin	0.196	2.75
3	Carboplatinum	9.25	42.33
4	Cytarabine	1.63	10
5	6-thioguanine	3.37	2.66
6	Ifosfamide	5.58	2.16
7	6Marcaptopurine	18	2.0
8	CNUU	26.83	2.133
9	Procarbazine	190	0.55

According to Fluda et al., Mitoxantrone, Belomycin, and Cisplatinum are highly effective drugs while Carboplatinum, Cytarabine, 6-thioguanine, and Ifosfamide exhibit intermediate effect and drugs including 6-Marcaptopurine, CCNU, and Procarbazine showed least effect against six NB cell lines indicated in the Table 4. Mitoxantrone, a synthetic anthracenedione, is an antineoplastic agent. It inhibits the activity of topoisomerase II, causes late S phase or G2/M phase cell arrest [113]. It was first developed in 1980s having decreased cardiotoxicity activity, effective against adult acute myeloid leukemia, symptomatics hormone-refractory prostate cancer, and relapsing multiple sclerosis [114]. Bleomycin, an antitumor drug, interfere with DNA synthesis

and causes DNA damage. It is highly cell cycle phase specific mainly effecting the late G1 phase or S phase of cell cycle [115]. It is effective against lymphoma, neck and head malignancy, and testicular tumor.

Carboplatinum inhibit the DNA synthesis by cross-linking of DNA strands, interferes with RNA transcription and causing the growth imbalance that eventually leads to cell death. It is used against ovarian cancer, other types of cancer include head and neck, lung, bladder, endometrial, esophageal, and cervical; osteogenic sarcoma, CNS or germ cell tumors [117]. Cytarabine, an antineoplastic agent belongs to the category of anthracyclines, used against leukemias and lymphomas. Cytarabine is pyrimidine analog, it competes with cystidine to incorporate itself into DNA and hinder the rotation of the molecule within DNA. It ceases the replication process during the S phase. It also stop the DNA replication process due to the inhibition of DNA polymerase [118]. 6-thioguanine, an antineoplastic anti-metabolite chemotherapy, used against acute myelogenous leukemia. It also exhibited anti-inflammatory and immunosuppressive effects. It is a purine analog of guanine that incorporate into DNA and RNA results in blockage of synthesis and metabolism of purine nucleotide [119]. Ifosfamide, an alkylating and immunosuppressive agent, cause the cell death by inter and intra strands ross-linking in DNA by binding with nucleic acid or other intracellular structures, also inhibit the DNA and protein synthesis. It is commonly used against lung cancer, bladder cancer, cancer of ovaries, certain soft tissues of brain sarcomas, and cervix cancer [120].

6-Marceptopurine, an antineoplastic anti-metabolite and immunosuppressive agent, inhibit the DNA synthesis by interfering with nucleic acid synthesis. It is commonly used to treat acute lymphocytic leukemia [121]. CCNU, an alkylating agent, stop the cell division by sticking to one of the cell's DNA strand. It is commonly used to treat brain tumors and also used in combination with other drugs to prepare people for stem cell or bone marrow transplant [122]. Procarbazine, an alkylating agent, used in combination with other drugs for stage III and IV Hodgkin's disease. Procarbazine is cell phase specific, causing S phase arrest. It stops the DNA replication by cross-linking guanine bases in DNA stands. The strands are unable to uncoil and separate, making them unable to divide [123].

In addition to incorporating drug effects, we also considered the impact of Ca^{2+} modulators on both Ca^{2+} signaling and cell growth. Thapsigargin (Tg), a SERCA pump inhibitor, is used in

this study. While Ca^{2+} plays a crucial role as a second messenger in cellular proliferation and differentiation, it also possesses the ability to act as a potent inducer of cell death. Various Ca^{2+} channels and pumps collaborate to ensure proper cellular function. SERCA, one of the Ca^{2+} pump, plays a critical role in maintaining a compartmentalized distribution of Ca^{2+} within the cell, thereby influencing Ca^{2+} signaling dynamics. Previous studies have examined the role of SERCA activity in cell proliferation and apoptosis, employing Tg as a valuable tool. It has been reported that by inhibiting the SERCA pump by Tg may leads to rapid depletion of the ER, subsequently triggering a cascade of secondary events. These events contribute to the activation of caspases, ultimately leading to cell death.

To examine the impact of Tg-mediated apoptosis, Nath *et al.* in 1997 used the NB cell line (NH-SY5Y) and fetal rate cortical cultures. They demonstrated that the loss of cell viability occurs within 24 to 48 hours when applying Tg at various concentrations (10nM to 1μM). After eight hours of Tg treatment, the DNA of these cells displayed the characteristic laddering pattern of oligonucleotides. One hour prior to the administration of Tg, they administered Dantrolene, an inhibitor of Ca^{2+}-induced Ca^{2+} release from ER, which lowers apoptosis by 40%. The exact mechanism causing apoptosis is unknown, although Nath *et al.* hypothesized that Tg-mediated ER Ca^{2+} depletion causes an increase in cytosolic Ca^{2+}, which triggers cell death pathways. Additionally, they also mentioned that Tg apoptosis is highly cell dependent [124]. Mary *et al.* did a further investigation into Tg-mediated cell death in 2005. They studied that Tg-induced ER stress activates caspase 2,3 and 7 in SH-SY5Y cells. They further examined the effect of cell-permeable caspase inhibitors on Tg-induced cell death. Among the caspase inhibitors used (Z-VDVAD-FMK, Z-DEVD-FMK, Z-LEHD-FMK, Z-VAD-FMK), Z-VAD-FMK was a potent inhibitor of Tg-stimulated cell death and showed 100% response, while other inhibitors showed 33, 11, and 16% response respectively [125].

Herein, we evaluated the response of drugs using the saturation equation, with data obtained from Fluda *et al.*'s study [112]. Likewise, the response of the modulator was derived from Sehgal *et al.*'s study [126]. They investigated the effects of Tg and its analogs on cell death through the inhibition of the SERCA pump. The study reported that Tg and its analogs, within various concentration ranges, inhibit SERCA 1a activity, leading to cell death caused by ER depletion.

The results of simulating the addition of drug and modulator responses in different cell cycle phases are presented in Table 5. Among the tested drugs, mitoxantrone exhibited the highest response, with a drug plasma level of 1.655 nmol/ml and an ED_{50} value of 0.06 nmol/ml. Following 15 days of treatment, the drug reduced the cell count from 34,324.81 to 398.04. On the other hand, when Tg response was simulated alone, the cell counts only decreased slightly from 34,324.81 to 34294.02, indicating that Tg alone had a negligible effect on the cell count. However, when both the drug and modulator were applied simultaneously, the cell count significantly decreased from 34,324.81 to 367.24. This suggests that the combined effect of the drug and modulator led to a substantial reduction in the cell count. The response of all the mentioned drugs, alone and in combination with Tg, was examined and is provided in Table 5. These findings highlight the effectiveness of mitoxantrone and the synergistic effect of combining the drug and modulator in achieving a significant reduction in cell count.

The graphical view in Figure 16(a) illustrates the sinusoidal behavior of mitoxantrone alone and in combination with Tg. Initially, mitoxantrone exhibits its maximum response by arresting cells in the G1 and G2/M phase, resulting in a reduction of the initial malignant cell count from 269.94 to 134.76 within approximately 72 hours. After 72 hours, the response of mitoxantrone started to decline, and an increased cell count of 361.00 was observed. When considering the synergistic effect of mitoxantrone and Tg, the cell count increased to 233.54 as the therapy's effect was minimized. This indicates that mitoxantrone alone showed slightly higher cell count, while when combined with Tg, the cell count decreases. The remaining cells then begin to proliferate as the response to chemotherapy reduces. This implies that as the chemotherapy's response decreases, the medication dose should be repeated after regular interval. The sinusoidal behavior of the curves demonstrates that the proposed chemotherapy does not completely eradicate the tumorigenic cells but helps to maintain the cell count at a reduced level. These curves also highlight the significant influence of Ca^{2+} signaling oscillation on the cell count when considering chemotherapeutic treatments.

Bleomycin, the second highest active drug, exhibited a similar sinusoidal behavior in terms of the cell count. The synergistic effect of bleomycin and Tg reduced the cell count from its initial value of 34,324.81 to 564.15, while bleomycin alone reduced the cell count to 594.94. The sinusoidal illustration in Figure 16(b) emphasizes the need for continuous chemotherapy

intervention to maintain the cell count at the lowest stable level. Carboplatinum, another chemotherapeutic drug, its inhibitory potency is less compared to the bleomycin, reduces the cell count from 34,324.81 to 1499.59 when administered alone, while in combination with Tg, the observed cell count is 1468.79. Figure 16(c) provides a graphical representation of the reduction in cell growth.
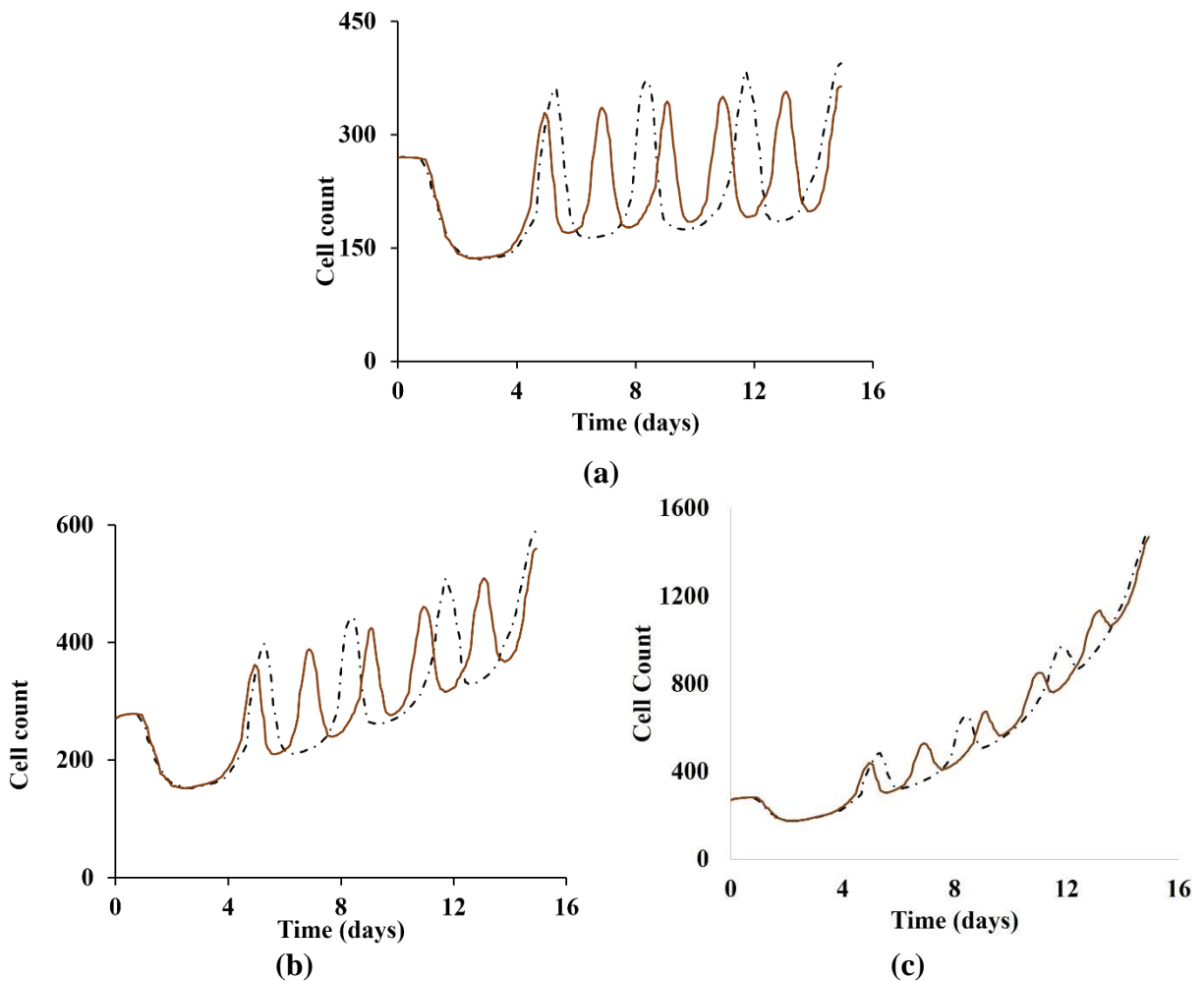

(a)

(b)   (c)

Figure 16: Graphical representation of the output of cell growth model while studying the effect of highly effective drugs and Ca^{2+} modulator Tg on SK-N-SH, both individually and in combination. (a) shows the effect of mitoxantrone alone and combined with Tg. The cure in black shows the effect of mitoxantrone on cell growth (represented as cell count) while the brown curve shows the combined effect of drug (mitoxantrone) and Ca^{2+} modulator (Tg) on cell growth. (b) represents the cell growth curves for drug bleomycin alone and in combined with Tg. The black curve represents the cell growth of drug only while brown curve shows the effect of bleomycin and Tg on cell growth. The effect of carboplatinum (shown in black curve) alone and in combined with Tg (shown in brown color) is represented in (c).

Similarly, drugs such as Cytarabine, 6-thioguanine, and Ifosfamide exhibit intermediate responses on cell growth in SK-N-SH cells. The reduction observed in the cell count is presented in Table 5, while Figure 17(a), (b), and (c) provide graphical visualizations of the respective drugs alone and in combination with Tg. Cytarabine and Tg changes cell count from 34,324.81 to 1076.37. Similarly, 6-thioguanine and Ifosfamide, along with Tg, result in decreases from 34,324.81 to 8117.50 and 17,964.93, respectively. As the drug's response diminishes, the curves in the graphical representation transitions to an exponential behavior. The decrease in sinusoidal curves suggests that as the impact of the drug on cell count decreases, the influence of Ca^{2+} signaling on the growth pattern of cells also decreases. The reason for this may be the diminished effectiveness of the Ca^{2+} modulator as the drug's activity decreases. Similar behavior is observed for the remaining two intermediate drugs, 6-thioguanine and ifosfamide. The graphical illustration of drug's response curves shows that as the drug's potency against SK-N-SH cells decreases, an approximate exponential behavior is observed, presented in Figure 17.
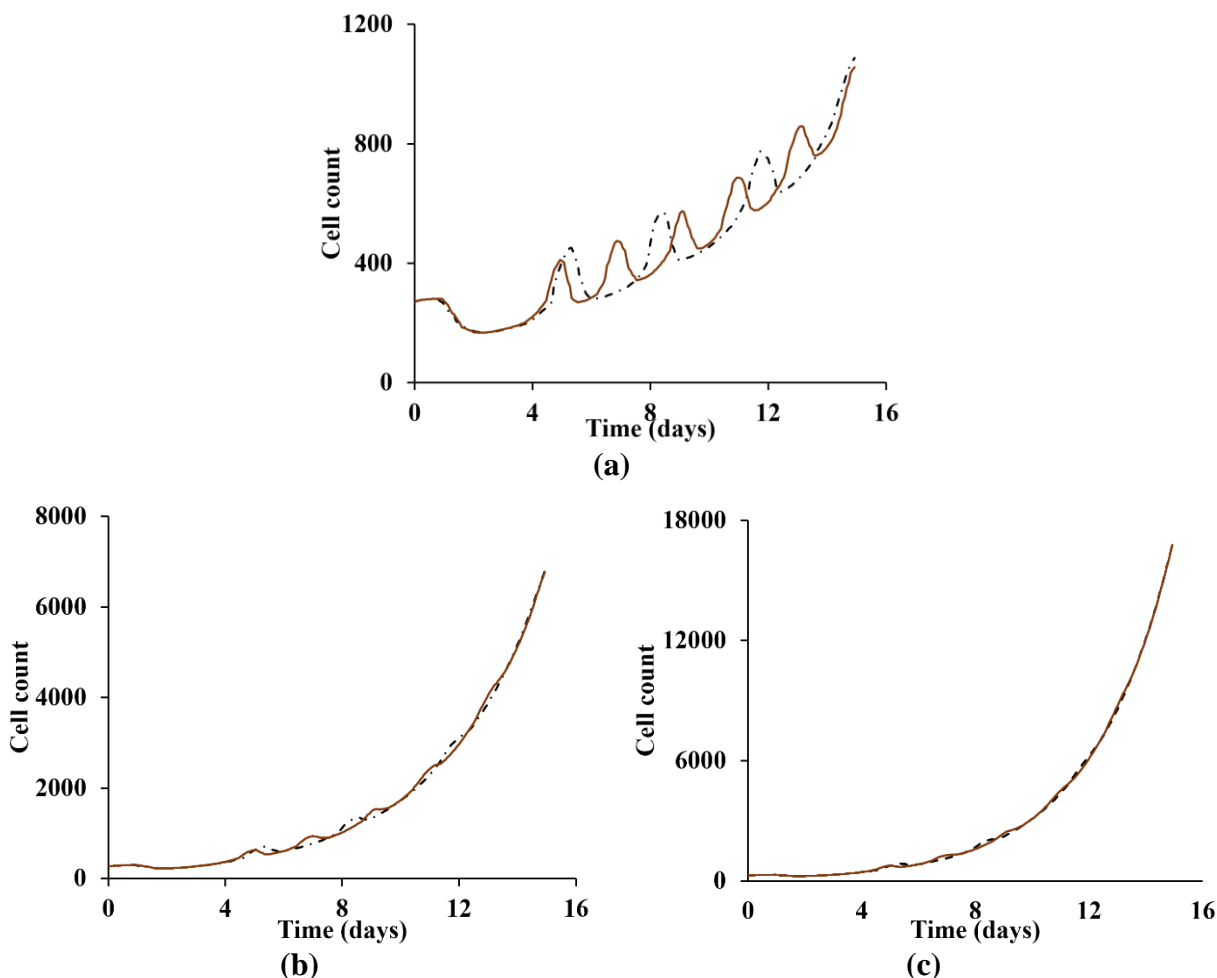
Figure 17: Graphical representation of the output of cell growth model while studying the effect of drugs with intermediate activity and Ca^{2+} modulator Tg against SK-N-SH, both individually and in combination. (a) shows the effect of cytarabine alone (black curve) and in combined with Tg (brown curve). The images (b) and (c) shows the cell growth curves for drugs 6-thioguanine and Ifosfamide alone (black curve) and in combined with Tg (brown curve) on SK-N-SH cells.

Lastly, drugs such as 6MP, CCNU, and procarbazine exhibited the lowest response when administered alone or in combination with Tg. The cell count decreased from 34,324.81 to 27,950.35, 27,049.38, and 34,139.12 when 6MP, CCNU, and Procarbazine were applied alone, respectively. Similarly, when combined with Tg, the cell count was 27,919.55, 27,018.59, and 34,108.32 respectively. These numbers indicate that there was no remarkable difference in the cell count before and after the application of chemotherapy. The graphical visualization in Figure 18(a), (b), and (c) illustrates the absence of significant differences in the response of the drugs alone and in combination with Tg. The exponential curves in these figures indicate that due to the

minimal response of the drugs, the modulator Tg also had no significant effect in reducing the growth of NB cells.
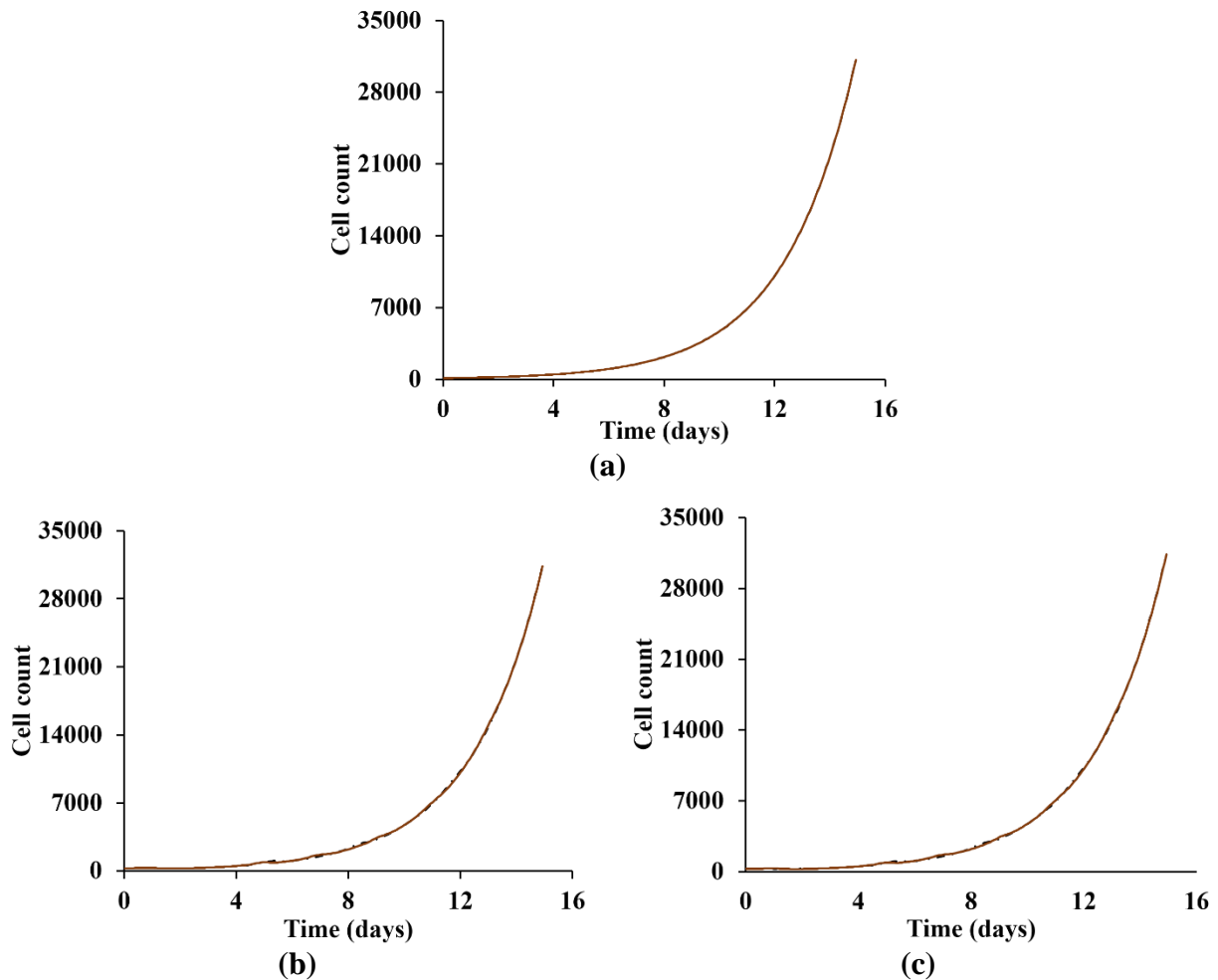

Figure 18: Graphical representation of the output of cell growth model while studying the effect of least active drugs and Ca^{2+} modulator Tg on SK-N-SH, both individually and in combination. The image (a) shows the effect of 6-MP (black curve) on cell growth alone and in combined with Tg (brown color). Similarly, the images (b) and (c) shows the effect of CCNU and Procarbazine (black curve in both cases) alone and in combined with Tg (brown curve) on cell growth in SK-N-SH cells.

Based on these results, we infer that drugs with a high response against SK-N-SH cells along with Tg improve the therapeutic effects. Highly active drugs along with Tg showed the sinusoidal growth depicting the dose repetition to maintain cell count as lower stable number. As the cytotoxic response of drug diminishes, a substantial decrease in sinusoidal pattern is observed. We depict that as the cytotoxic effect of drug decreases, the influence of Tg on cell growth pattern also decreases, thus changing the growth pattern from sinusoidal to exponential with increased cell

count. This shows the influence of Ca^{2+} signaling in regulating cellular growth. The proposed treatment approach can help maintain malignant cells at their lowest count and prevent metastasis to other organs. Surgical treatments may be applied after chemotherapy to eliminate tumor cells from the affected organ.

Table 5

Summary of cell count after drugs response only, modulator response only, and drug & modulator response on SK-N-SH cell line after 15 days of treatment.

Sr. no	Drug name	Drug response	Modulator response	Cell count after Drug response	Cell count after Ca^{2+} modulator response	Cell count after drug & modulator response
1	Mitoxantrone	0.96	0.80	398.04	34294.02	367.24
2	Bleomycin	0.93	0.80	594.9475	34294.02	564.1505
3	Carboplatinum	0.82	0.80	1499.593	34294.02	1468.796
4	Cytarabine	0.85	0.80	1107.172	34294.02	1076.375
5	6-thioguanine	0.44	0.80	8148.301	34294.02	8117.503
6	Ifosfamide	0.27	0.80	17995.72	34294.02	17964.93
7	6MP	0.10	0.80	27950.35	34294.02	27919.55
8	CNUU	0.07	0.80	27049.38	34294.02	27018.59
9	Procarbazine	0.01	0.80	34139.12	34294.02	34108.32

4.1 Local Sensitivity Analysis (LSA)

To access the relative significance of each kinetic parameter on cell growth, in the presence and absence of treatment, we performed local sensitivity analysis by perturbing the kinetic parameter of the cell growth model. The effect of the local perturbation on the kinetic parameters of the cell growth model keeping initial values fixed is presented in subsection A.1 while subsection A.2 contains the perturbation in initial conditions keeping other kinetic parameters fixed.

4.1.1 LSA of Kinetic parameters

The local sensitivity analysis for the kinetic parameters given in Table 2 is conducted by perturbing each parameter individually by a small amount and predicting its effect on cell count. The following formula is used to calculate relative sensitivity.

$$Relative\ sensitivity = \frac{(perturbed_{output} - baseline_{output})}{baseline_{output}} * 100 \quad (22)$$

$perturbed_{output}$ is the predicted output when the perturbed input parameters are applied, while $baseline_{output}$ is the nominal output when no perturbation is applied. The kinetic parameters in Table 2 are perturbed one by one and their influence on cell count is checked both in the normal and cancerous condition. The graphical illustration given in Figure 20 shows that the cell growth model is more sensitive to the parameters representing the transition rates between phases in normal and tumorigenic conditions. It is observed from the figure that in tumorigenic condition, c_1 shows an increased sensitivity compared to c_s and c_2. Likewise, in normal cell growth, the increased and decreased perturbation in transition parameters increases the relative sensitivity to the growth model but the observed percentage increase is less than the tumor cells. From the graphical illustration, we infer that the transition parameters in tumor cells are more sensitive to perturbation compared to normal cells. Parameters x_1, x_2, and x_3 are perturbed by a 10% increase and decrease from their baseline values, a negligible sensitivity to the growth model is observed in both the normal cells and the SK-N-SH cells.
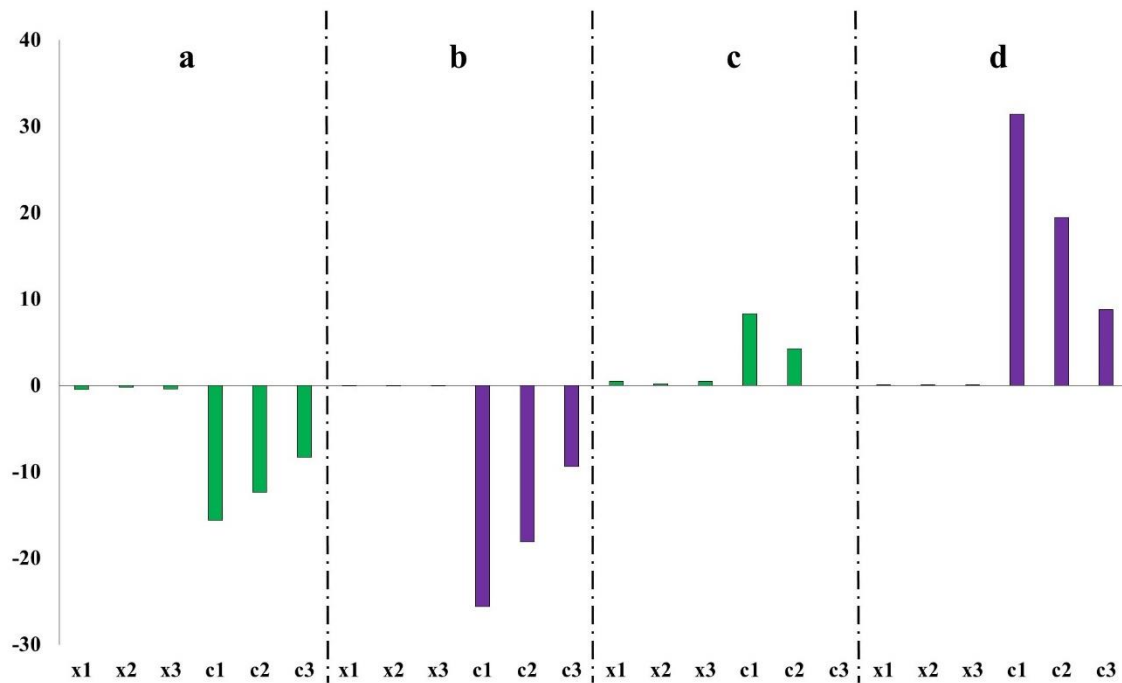
Figure 20: Local sensitivity analysis of the kinetic parameters used in ODEs (from 8-10) for cellular growth prediction in the normal cells and Nb SK-N-SH cell line. The parameters are presented on the x-axis while the y-axis shows the relative sensitivity. (a) represented the 10% decreased perturbation in kinetic parameters for normal cell growth while (b) shows the 10% decreased perturbation in SK-N-SH cell growth. Likewise, (c) and (d) represented the 10% increased perturbation in kinetic parameters of cellular growth models in normal and SK-N-SH cell line.

In the next section, we perturbed growth parameters when highly active, intermediate, and least active drugs are given in the presence and absence of a Ca^{2+} modulator. Figure 21 shows the relative sensitivity of cell growth parameters when 10% increased (a) and decreased (b) perturbations are applied. It is clear from the figure that the parameters x_1, x_2, and x_3 are more sensitive to the perturbation when the highly active drug is given alone or in combination with Tg. Likewise, the negative perturbation in growth parameters shows negative sensitivity to the cellular growth model. However, x_1 demonstrates a slight positive effect on tumor growth in 10% decreased perturbation. The produced behavior is opposite when compared with SK-N-SH's growth in the absence of treatment (Figure 20(b)(d)), which depicts the higher relative sensitivity of the parameter showing Ca^{2+} concentration in cell cycle compartments.
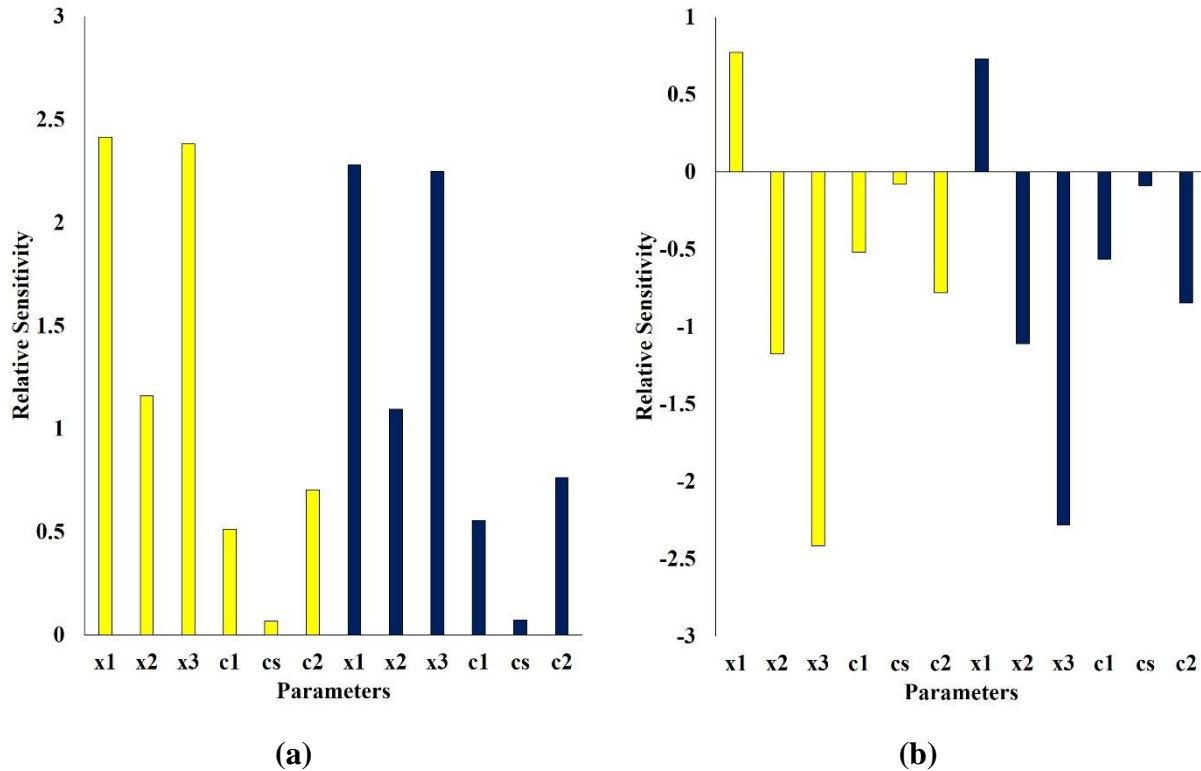
Figure 21: Sensitivity analysis of cell growth parameters in the presence of highly active drug mitoxantrone (green color) and in the presence of both mitoxantrone and Tg (blue color). (a) showed when parameters are perturbed by 10% increase in its baseline values while (b) showed the 10% decrease in parameter values form its baseline value.

The effect of local sensitivity analysis in the presence of 6-thioguanone alone and in combined with Tg is presented in Figure 22. The increased (a)(b) and decreased (c)(d) perturbations in growth parameters shows that c_1, c_s and c_2 have significant effect on SK-N-SH cells compared to other growth parameters.
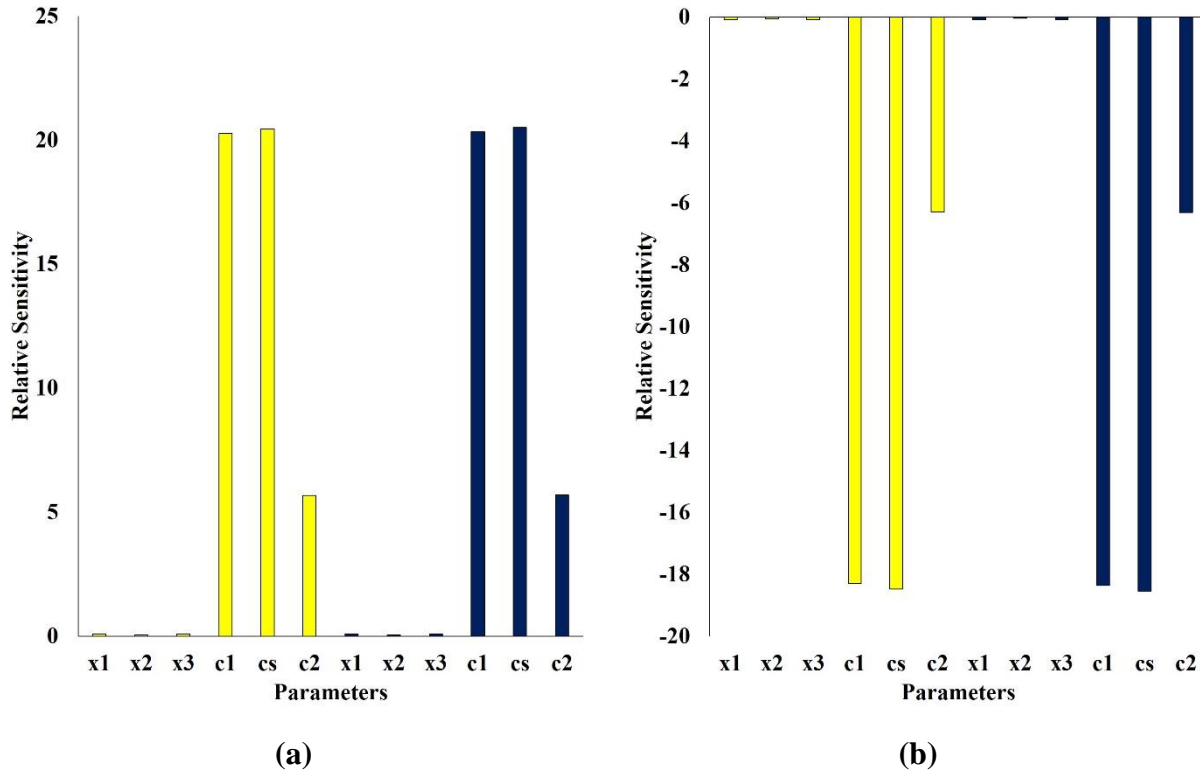
(a) **(b)**

Figure 22: Sensitivity analysis of growth model parameters when 6-thioguanine drugs (in green color) is applied alone or in combination with Tg (blue color). (a) showed the 10% increase in cell growth parameters values from its baseline value while (b) showed 10% decrease in cell growth parameters values.

Lastly, we checked the effect in parameter perturbation when procarbazine alone or in combined with Tg is applied. The Figure 23 shows that during the 10% increased perturbations, the SK-N-SH's growth is more sensitive to c_1, c_s while c_2 has no impact on growth. Likewise, during the 10% decreased perturbation, parameter c_1 shown more sensitivity compared with c_s while c_2. Other growth parameters including x_1, x_2, and x_3 have no impact on SK-N-SH growth.

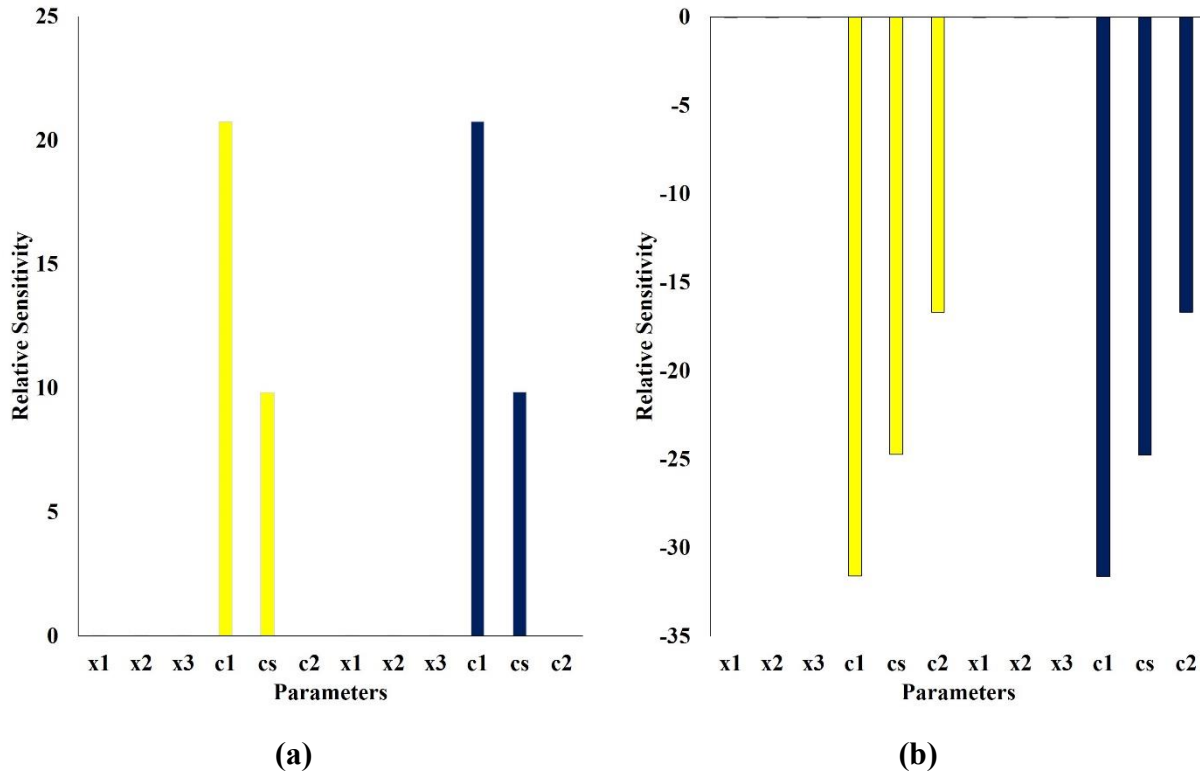(a)   (b)

Figure 23: Sensitivity analysis of cell growth model in the presence of least effective drug, procarbazine. The green color showed the relative sensitivity (10% increases or decrease) of parameters in the presence of drug only while purple color showed the relative sensitivity (10% increases or decrease) of parameters in the presence of combined therapy.

From these results, we infer that when highly active drugs are given, the growth model becomes more sensitive to the Ca^{2+} regulating parameters as compared to the other growth parameters, depicting the strong influence of Ca^{2+} signaling on cell's growth. Similarly, when drugs with low response against SK-N-SH are applied to the cell growth model, the sensitivity of parameters showing transition rates between phases increases compared to the other growth parameters.

4.1.2   LSA of Initial Conditions

In this section, we analyze the effect of perturbation in the initial conditions of the cell growth model when no treatment, single therapy, and combined therapy is applied. Each initial condition is perturbed by 10% increase and decrease keeping all other kinetic parameters constants. Equation 22 is used to compute the model's relative sensitivity to the initial conditions. The graphical illustration is presented in Figure 24 showed the increased or decreased perturbation leads to

different sensitivity of each initial condition to the SK-N-SH's growth. The perturbations in G phase showed the significant sensitivity to the tumor growth as compared to other phases.
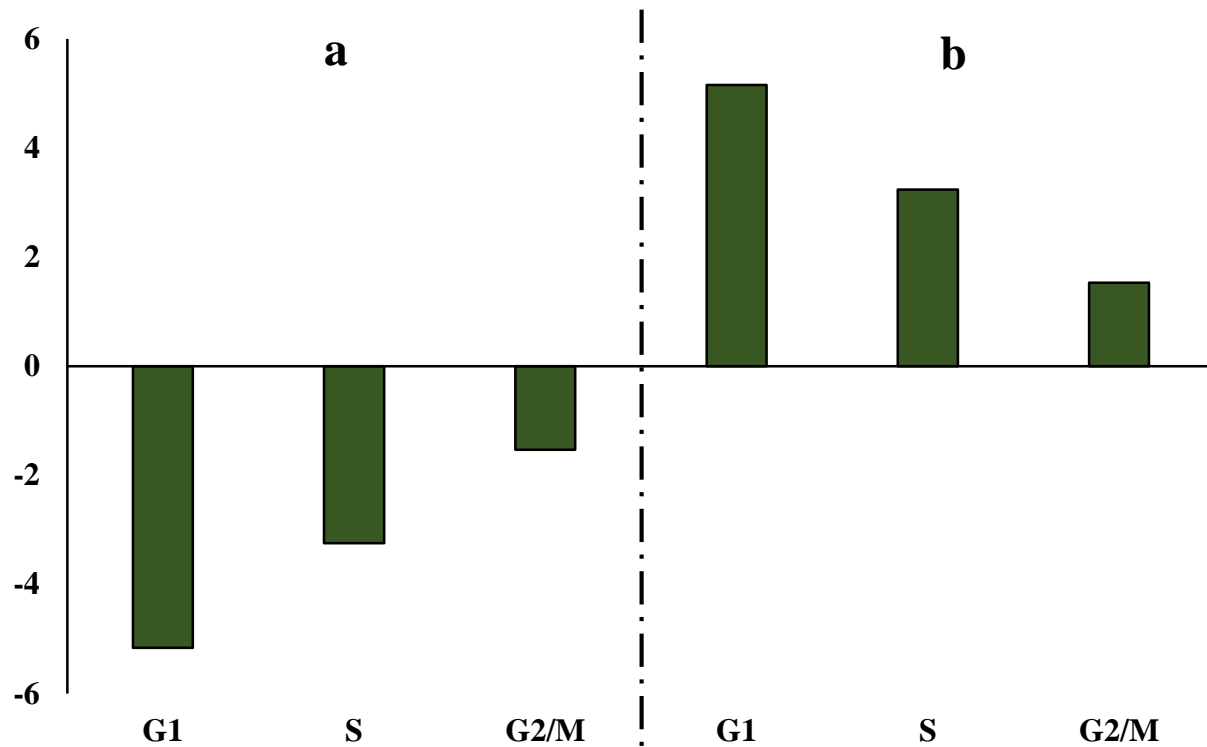
Figure 24: Local sensitivity analysis in the initial conditions of growth model keeping other growth parameters constant in the absence of treatment. (a) shows the 10% decreased perturbation in initial conditions while (b) shows the 10% increased perturbation in initial conditions.

We also observed effect of increased or decreased perturbation in initial conditions when highly active, intermediate, and least active drugs are applied to check their cytotoxic effect on cellular growth.

Figure 25: Local senistivity analysis of initial conditions when highly active drug (mixantrone) is applied along with Tg as cytotoxic agent on SK-N-SH cells. X-axis represnets the parameters while y-axis shows the relative sensitivity of pertrubed parameters.

Figure 26: Local senistivity analysis of initial conditions when drug showing intermediate effect (6-thioguanine) is applied along with Tg as cytotoxic agent on SK-N-SH cells. X-axis represnets the parameters while y-axis shows the relative sensitivity of pertrubed parameters.
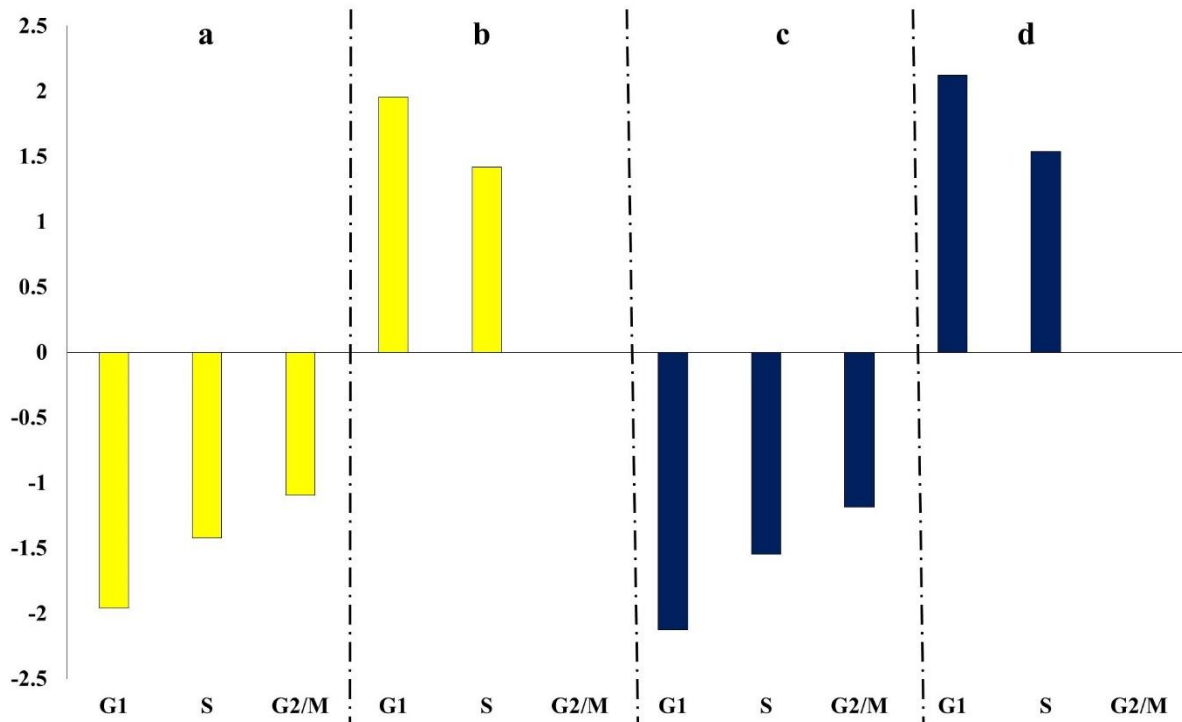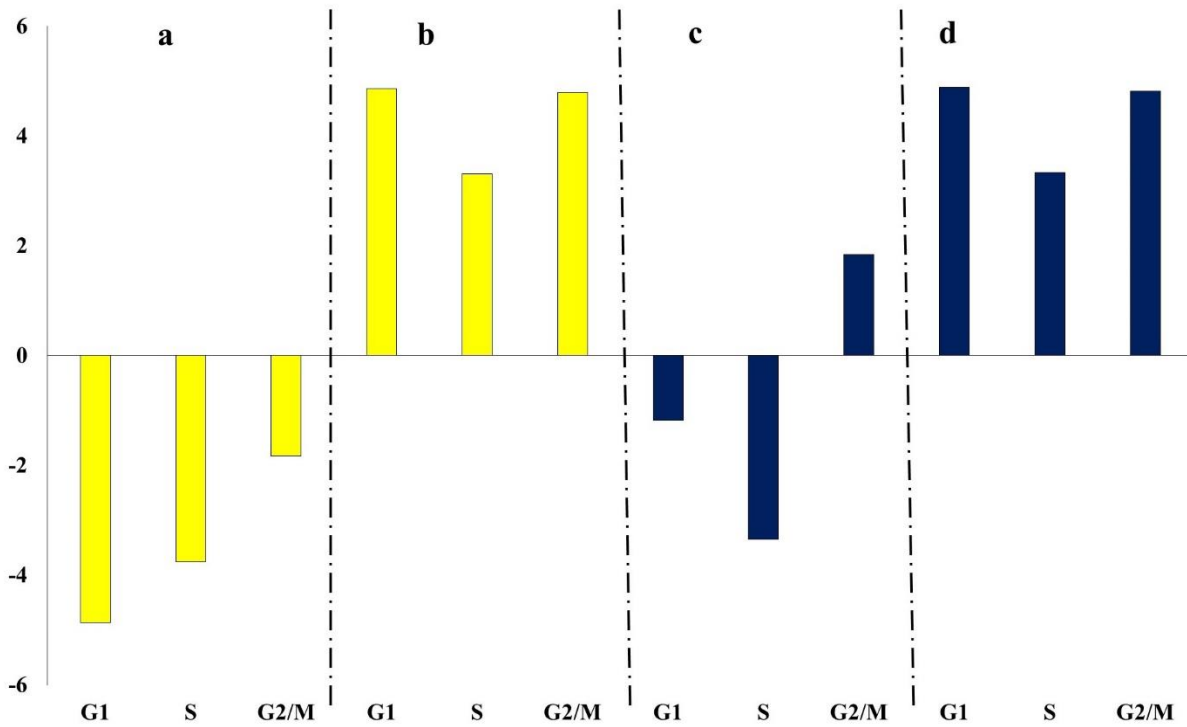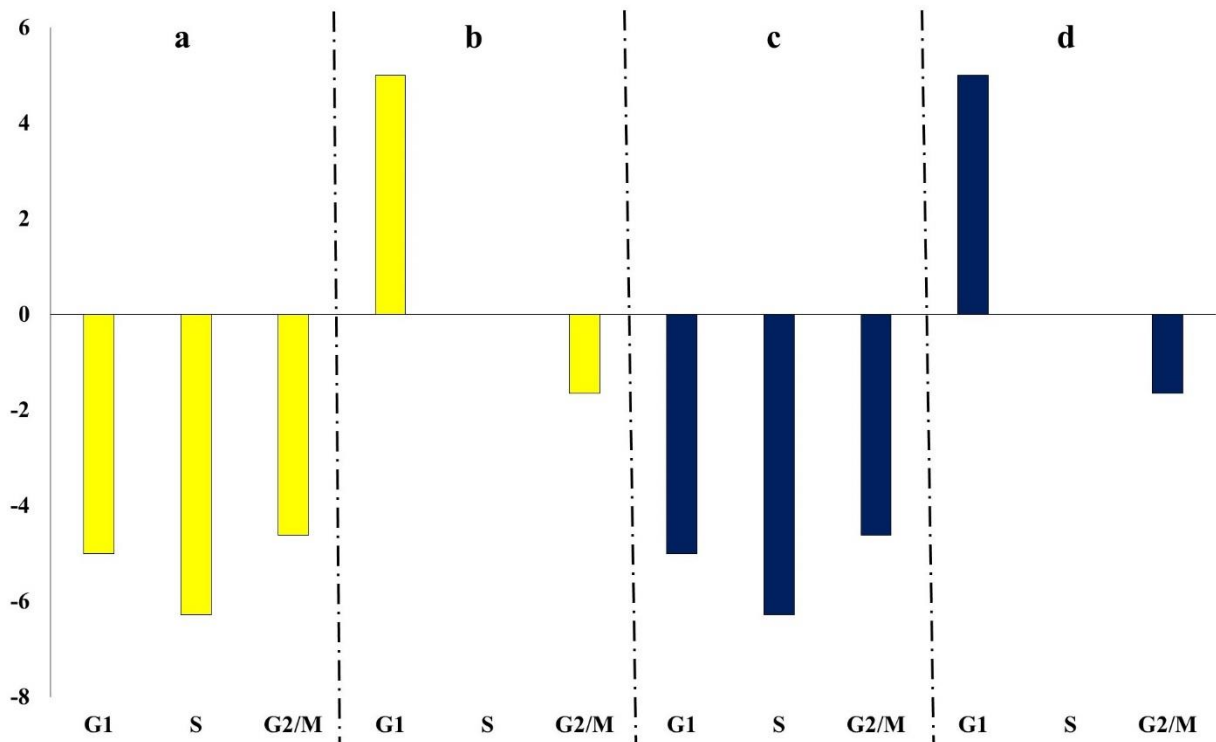
Figure 27: Local senistivity analysis of initial conditions when least active drug (procarbazine) is applied along with Tg as cytotoxic agent on SK-N-SH cells. X-axis represnets the parameters while y-axis shows the relative sensitivity of pertrubed parameters.

The graphical illustration presented in Figure 25 shows that there is a significant impact of perturbing parameters when comparing the treatment versus no treatment (see Figure 24(a) and (b)). The 10% increased perturbation in G1 phase, when mitoxantrone (b) alone and combined with Tg (d) is applied, demonstrate greater sensitivity to the SK-N-SH growth than the S phase, while G2/M phase remains insensitive after perturbation. Similarly, a 10% decreased perturbation shows that G1 phase has more impact on SK-N-SH growth compared to S and G2/ M phases (Figure 25(a) and (b).

Similarly, the local sensitivity analysis of drug having intermediate response on SH-N-SH's growth is presented in Figure 26 shows that the growth model is more sensitive to the perturbation in G1 and G2/M phase as compared to the S phase. The effect of 10% deceased and increased perturbation in the presence of 6-thioguanine (a)(b) demonstrate that perturbation in G1 and G2/M phases are more sensitive to SK-N-SH growth compared to the S phase. When the local

sensitivity analysis of increased and decreased perturbation is studied in combined chemotherapy that is 6-thioguanine and Tg (Figure 26(c) and (d)), slightly different response is observed compared to the 6-thioguanine alone. It is observed that decreased perturbation in S phase is more sensitive to SK-N-SH growth compared to G1 phase while G2/M phase demonstrate positive effect on SK-N-SH growth.

Lastly, we studied the impact of decreased and increased perturbation when the least sensitive drug procarbazine alone (Figure 27 (a)(b)) and in combined with Tg (Figure 27(c)(d)) is applied. The figure shows that in decreased perturbation, the S phase is more sensitive compared to G1 and G2/M phases while during the increased perturbations, the G1 phase imparts a significant impact compared to the G2/M phase and the S phase has no impact on SK-N-SH growth. From the local sensitivity analysis of different growth parameters in the presence and absence of chemotherapy (single and combined), we can get an idea of important and sensitive parameters that impart a significant impact on the relative growth of SK-N-SK and normal cells. This process could help in parameter extraction and optimization.

4.2   Applicability of the proposed methodology

Lead optimization programs help in the refinement of potential hits to the leads that possess the drug-like properties, safety profiles, and selectivity to progress from preclinical and clinical testing and to be used as a potential drug candidate. Currently, different methodologies like molecular docking and simulation, SAR, 2D/3D QSAR, pharmacophore modeling, and machine learning/deep learning methods are employed to predict drug efficacy against specific targets. Lead optimization programs help in the structure and dose optimization process ensuring the maximum response of drug with less toxicity. The predicted optimized dose is then tested in preclinical and clinical trials to study its effect against specific cell lines. The proposed mathematical model can be used as a tool for dose optimization against specific cell lines (NB, in our case). The predicted potency of potential leads could be screened from the proposed mathematical model and their response on the cellular growth of NB could be evaluated.

4.3   Limitations and Future Directions

This study has several limitations that should be taken cautiously. Firstly, the simulated results obtained through the proposed methodology provide valuable insights into the general behavior of

disease dynamics and the predicted outcomes of drugs and Ca^{2+} modulators with different responses against SK-N-SH cells. However, due to the *in-silico* nature of the process, these simulated results cannot be directly utilized for making medical decisions. They should be interpreted as theoretical predictions that can inform and guide medical professionals in designing optimal treatment protocols. Furthermore, while the models are built upon parameter values derived from *in-vitro* or *in-vivo* results, it is important to note that they are not patient-specific. Personalized mathematical models can be developed by incorporating patient-specific data, which could assist in making decisions regarding optimal treatment strategies based on an individual's specific genetic makeup.

Another limitation of the proposed methodology is that the deterministic mathematical model used was unable to accurately simulate the shape of Ca^{2+} oscillations. In future research, it would be beneficial to enhance the model by incorporating spatial effects, stochasticity, and additional biochemical reactions. These modifications would allow for a more precise simulation of Ca^{2+} oscillations and cell cycle growth. Despite these limitations, the proposed models hold promise for evaluating the impact of Ca^{2+} signaling and combined therapeutics. The present study could aid in the selection of drugs and Ca^{2+} modulators that achieve the desired efficacy at lower concentrations. It is important to continue refining and expanding these models to improve their accuracy and applicability in clinical decision-making processes.

Chapter 5

Conclusions

Previous studies extensively define the role of intracellular Ca^{2+} in regulating cellular processes. Additionally, various therapeutics targeting Ca^{2+} dynamics are being explored to address different pathophysiological conditions. In this study, we modified the previously proposed Ca^{2+} dynamic model and optimized their parameters to capture the general behavior of Ca^{2+} signaling under normal and diseased conditions. Tumorigenic cells displayed elevated Ca^{2+} amplitude compared to normal cells. These results were integrated into the cellular growth model of Wallace *et al.*, extending the study duration to 15 days. The model predicted uncontrolled growth in SK-N-SH cells, with cell counts reaching $34,324*10^6$, while normal cells contained $1912*10^6$ cells after 15 days. When incorporating the response of chemotherapeutic drugs and Ca^{2+} modulators, a significant decrease in cell count was observed. The simulation results showed that in NB, chemotherapy of anti-cancer drugs along with a modulator of Ca^{2+} concentration may demonstrate superior outcomes compared to individual chemotherapy approaches. Furthermore, highly active drugs were found to be crucial for Ca^{2+} modulators to induce notable effects on cell growth. The local sensitivity analysis revealed the importance of Ca^{2+} regulating parameters in the growth models of SK-N-SK NB cells and normal cells. Likewise, kinetics parameters showing the transition rates between phases hold significance when the least active drugs were used.

Reference

1. Gurney JG, Ross JA, Wall DA, Bleyer WA, Severson RK, Robison LL. Infant Cancer in the U.S.: Histology-Specific Incidence and Trends, 1973 to 1992. J Pediatr Hematol Oncol. 1997;19:428–32.

2. Cohn SL, Pearson ADJ, London WB, Monclair T, Ambros PF, Brodeur GM, et al. The International Neuroblastoma Risk Group (INRG) Classification System: An INRG Task Force Report. J Clin Oncol. 2009;27:289–97.

3. Smith V, Foster J. High-Risk Neuroblastoma Treatment Review. Children. 2018;5:114.

4. Matthay KK, Maris JM, Schleiermacher G, Nakagawara A, Mackall CL, Diller L, et al. Neuroblastoma. Nat Rev Dis Primer. 2016;2:16078.

5. Tsai H-C, Baylin SB. Cancer epigenetics: linking basic biology to clinical medicine. Cell Res. 2011;21:502–17.

6. Cohen LE, Gordon JH, Popovsky EY, Gunawardene S, Duffey-Lind E, Lehmann LE, et al. Late effects in children treated with intensive multimodal therapy for high-risk neuroblastoma: High incidence of endocrine and growth problems. Bone Marrow Transplant. 2014;49:502–8.

7. Fati F, Pulvirenti R, Paraboschi I, Martucciello G. Surgical Approaches to Neuroblastoma: Review of the Operative Techniques. Children. 2021;8:446.

8. Hobbie WL, Moshang T, Carlson CA, Goldmuntz E, Sacks N, Goldfarb SB, et al. Late effects in survivors of tandem peripheral blood stem cell transplant for high-risk neuroblastoma. Pediatr Blood Cancer. 2008;51:679–83.

9. Polishchuk AL, DuBois SG, Haas-Kogan D, Hawkins R, Matthay KK. Response, survival, and toxicity after iodine-131-metaiodobenzylguanidine therapy for neuroblastoma in preadolescents, adolescents, and adults. Cancer. 2011;117:4286–93.

10. Lee JS, Padilla B, DuBois SG, Oates A, Boscardin J, Goldsby RE. Second malignant neoplasms among children, adolescents and young adults with Wilms tumor. Pediatr Blood Cancer. 2015;62:1259–64.

11. Cuthbertson KSR, Cobbold PH. Phorbol ester and sperm activate mouse oocytes by inducing sustained oscillations in cell Ca2+. Nature. 1985;316:541–2.

12. Monteith GR, Prevarskaya N, Roberts-Thomson SJ. The calcium–cancer signalling nexus. Nat Rev Cancer. 2017;17:373–80.

13. Satheesh N, Büsselberg D. The Role of Intracellular Calcium for the Development and Treatment of Neuroblastoma. Cancers. 2015;7:823–48.

14. Abid MdR, Guo S, Minami T, Spokes KC, Ueki K, Skurk C, et al. Vascular Endothelial Growth Factor Activates PI3K/Akt/Forkhead Signaling in Endothelial Cells. Arterioscler Thromb Vasc Biol. 2004;24:294–300.

15. Opel D, Poremba C, Simon T, Debatin K-M, Fulda S. Activation of Akt Predicts Poor Outcome in Neuroblastoma. Cancer Res. 2007;67:735–45.

16. Passoni L, Longo L, Collini P, Coluccia AML, Bozzi F, Podda M, et al. Mutation-Independent Anaplastic Lymphoma Kinase Overexpression in Poor Prognosis Neuroblastoma Patients. Cancer Res. 2009;69:7338–46.

17. Eggert A, Ikegaki N, Liu X, Brodeur GM. Prognostic and Biological Role of Neurotrophin-Receptor TrkA and TrkB in Neuroblastoma1. Klin Pädiatr. 2000;212:200–5.

18. Chen H-J, Rojas-Soto M, Oguni A, Kennedy MB. A Synaptic Ras-GTPase Activating Protein (p135 SynGAP) Inhibited by CaM Kinase II. Neuron. 1998;20:895–904.

19. Egea J, Espinet C, Soler RM, Peiró S, Rocamora N, Comella JX. Nerve Growth Factor Activation of the Extracellular Signal-Regulated Kinase Pathway Is Modulated by Ca $^{2+}$ and Calmodulin. Mol Cell Biol. 2000;20:1931–46.

20. Viard P, Butcher AJ, Halet G, Davies A, Nürnberg B, Heblich F, et al. PI3K promotes voltage-dependent calcium channel trafficking to the plasma membrane. Nat Neurosci. 2004;7:939–46.

21. Matthay KK, Villablanca JG, Seeger RC, Stram DO, Harris RE, Ramsay NK, et al. Treatment of High-Risk Neuroblastoma with Intensive Chemotherapy, Radiotherapy, Autologous Bone Marrow Transplantation, and 13- *cis* -Retinoic Acid. N Engl J Med. 1999;341:1165–73.

22. Assuncao Guimaraes C, Linden R. Programmed cell deaths. Apoptosis and alternative deathstyles. Eur J Biochem. 2004;271:1638–50.

23. Halestrap AP, Doran E, Gillespie JP, O'Toole A. Mitochondria and cell death. Biochem Soc Trans. 2000;28:170–7.

24. Kerkhofs M, Bittremieux M, Morciano G, Giorgi C, Pinton P, Parys JB, et al. Emerging molecular mechanisms in chemotherapy: Ca2+ signaling at the mitochondria-associated endoplasmic reticulum membranes. Cell Death Dis. 2018;9:334.

25. Chen L, Iraci N, Gherardi S, Gamble LD, Wood KM, Perini G, et al. p53 Is a Direct Transcriptional Target of MYCN in Neuroblastoma. Cancer Res. 2010;70:1377–88.

26. Florea A-M, Büsselberg D. Cisplatin as an Anti-Tumor Drug: Cellular Mechanisms of Activity, Drug Resistance and Induced Side Effects. Cancers. 2011;3:1351–71.

27. Florea A-M, Büsselberg D. Anti-cancer drugs interfere with intracellular calcium signaling. NeuroToxicology. 2009;30:803–10.

28. Walter L, Hajnóczky G. Mitochondria and Endoplasmic Reticulum: The Lethal Interorganelle Cross-Talk. J Bioenerg Biomembr. 2005;37:191–206.

29. Parfitt AM. Calcium Homeostasis. Physiol Pharmacol Bone [Internet]. Berlin, Heidelberg: Springer Berlin Heidelberg; 1993 [cited 2023 Jun 21]. p. 1–65. Available from: http://link.springer.com/10.1007/978-3-642-77991-6_1

30. Nordin BEC, Peacock M. Role of Kidney in Regulation of Plasma-Calcium. The Lancet. 1969;294:1280–3.

31. Endo M. Calcium Ion as a Second Messenger With Special Reference to Excitation-Contraction Coupling. J Pharmacol Sci. 2006;100:519–24.

32. Dupont G, Falcke M, Kirk V, Sneyd J. Models of Calcium Signalling [Internet]. Cham: Springer International Publishing; 2016 [cited 2023 Jun 21]. Available from: http://link.springer.com/10.1007/978-3-319-29647-0

33. Schneider G, Oswald F, Wahl C, Greten FR, Adler G, Schmid RM. Cyclosporine Inhibits Growth through the Activating Transcription Factor/cAMP-responsive Element-binding Protein Binding Site in the Cyclin D1 Promoter. J Biol Chem. 2002;277:43599–607.

34. Roderick HL, Cook SJ. Ca2+ signalling checkpoints in cancer: remodelling Ca2+ for cancer cell proliferation and survival. Nat Rev Cancer. 2008;8:361–75.

35. Elmore S. Apoptosis: A Review of Programmed Cell Death. Toxicol Pathol. 2007;35:495–516.

36. Bruce JIE, James AD. Targeting the Calcium Signalling Machinery in Cancer. Cancers. 2020;12:2351.

37. Prevarskaya N, Skryma R, Shuba Y. Calcium in tumour metastasis: new roles for known actors. Nat Rev Cancer. 2011;11:609–18.

38. Keefe SM, Cohen MA, Brose MS. Targeting Vascular Endothelial Growth Factor Receptor in Thyroid Cancer: The Intracellular and Extracellular Implications. Clin Cancer Res. 2010;16:778–83.

39. Liedtke W, Kim C. Functionality of the TRPV subfamily of TRP ion channels: add mechano-TRP and osmo-TRP to the lexicon! Cell Mol Life Sci CMLS. 2005;62:2985–3001.

40. Petrova V, Annicchiarico-Petruzzelli M, Melino G, Amelio I. The hypoxic tumour microenvironment. Oncogenesis. 2018;7:10.

41. Rizzuto R, Pinton P, Ferrari D, Chami M, Szabadkai G, Magalhães PJ, et al. Calcium and apoptosis: facts and hypotheses. Oncogene. 2003;22:8619–27.

42. Azimi I. The interplay between HIF-1 and calcium signalling in cancer. Int J Biochem Cell Biol. 2018;97:73–7.

43. Shaw PJ, Weidinger C, Vaeth M, Luethy K, Kaech SM, Feske S. CD4+ and CD8+ T cell–dependent antiviral immunity requires STIM1 and STIM2. J Clin Invest. 2014;124:4549–63.

44. Dupont G, Falcke M, Kirk V, Sneyd J. Models of Calcium Signalling [Internet]. Cham: Springer International Publishing; 2016 [cited 2023 Jun 21]. Available from: http://link.springer.com/10.1007/978-3-319-29647-0

45. Mahama PA, Linderman JJ. Calcium signaling in individual BC3H1 cells: Speed of calcium mobilization and heterogeneity. Biotechnol Prog. 1994;10:45–54.

46. Falkenburger BH, Jensen JB, Hille B. Kinetics of M1 muscarinic receptor and G protein signaling to phospholipase C in living cells. J Gen Physiol. 2010;135:81–97.

47. Falkenburger BH, Jensen JB, Hille B. Kinetics of PIP2 metabolism and KCNQ2/3 channel regulation studied with a voltage-sensitive phosphatase in living cells. J Gen Physiol. 2010;135:99–114.

48. De Lean A, Stadel JM, Lefkowitz RJ. A ternary complex model explains the agonist-specific binding properties of the adenylate cyclase-coupled beta-adrenergic receptor. J Biol Chem. 1980;255:7108–17.

49. Weiss JM, Morgan PH, Lutz MW, Kenakin TP. The Cubic Ternary Complex Receptor-Occupancy Model III. Resurrecting Efficacy. J Theor Biol. 1996;181:381–97.

50. Lemon G, Gibson WG, Bennett MR. Metabotropic receptor activation, desensitization and sequestration—I: modelling calcium and inositol 1,4,5-trisphosphate dynamics following receptor activation. J Theor Biol. 2003;223:93–111.

51. MacLennan DH, Rice WJ, Green NM. The Mechanism of Ca2+ Transport by Sarco(Endo)plasmic Reticulum Ca2+-ATPases. J Biol Chem. 1997;272:28815–8.

52. Keener J, Sneyd J, editors. Mathematical Physiology [Internet]. New York, NY: Springer New York; 2009 [cited 2023 Jun 21]. Available from: http://link.springer.com/10.1007/978-0-387-75847-3

53. Tran K, Smith NP, Loiselle DS, Crampin EJ. A Thermodynamic Model of the Cardiac Sarcoplasmic/Endoplasmic Ca2+ (SERCA) Pump. Biophys J. 2009;96:2029–42.

54. Ji Y, Loukianov E, Loukianova T, Jones LR, Periasamy M. SERCA1a can functionally substitute for SERCA2a in the heart. Am J Physiol-Heart Circ Physiol. 1999;276:H89–97.

55. Hilgemann DW, Nicoll DA, Philipson KD. Charge movement during Na^+ translocation by native and cloned cardiac Na+/Ca2+ exchanger. Nature. 1991;352:715–8.

56. Hilgemann DW. New insights into the molecular and cellular workings of the cardiac Na^+/Ca^{2+} exchanger. Am J Physiol-Cell Physiol. 2004;287:C1167–72.

57. Jin C, Kumar P, Gracia-Sancho J, Dufour J. Calcium transfer between endoplasmic reticulum and mitochondria in liver diseases. FEBS Lett. 2021;595:1411–21.

58. Magnus G, Keizer J. Minimal model of beta-cell mitochondrial Ca2+ handling. Am J Physiol-Cell Physiol. 1997;273:C717–33.

59. Magnus G, Keizer J. Model of β-cell mitochondrial calcium handling and electrical activity. I. Cytoplasmic variables. Am J Physiol-Cell Physiol. 1998;274:C1158–73.

60. Cortassa S, Aon MA, Marbán E, Winslow RL, O'Rourke B. An Integrated Model of Cardiac Mitochondrial Energy Metabolism and Calcium Dynamics. Biophys J. 2003;84:2734–55.

61. Nguyen M-HT, Jafri MS. Mitochondrial Calcium Signaling and Energy Metabolism. Ann N Y Acad Sci. 2005;1047:127–37.

62. Patterson M, Sneyd J, Friel DD. Depolarization-induced Calcium Responses in Sympathetic Neurons: Relative Contributions from Ca2+ Entry, Extrusion, ER/Mitochondrial Ca2+ Uptake and Release, and Ca2+ Buffering. J Gen Physiol. 2007;129:29–56.

63. Marhl M, Haberichter T, Brumen M, Heinrich R. Complex calcium oscillations and the role of mitochondria and cytosolic proteins. Biosystems. 2000;57:75–86.

64. Csordás G, Hajnóczky G. Plasticity of Mitochondrial Calcium Signaling. J Biol Chem. 2003;278:42273–82.

65. Dash RK, Qi F, Beard DA. A Biophysically Based Mathematical Model for the Kinetics of Mitochondrial Calcium Uniporter. Biophys J. 2009;96:1318–32.

66. Wingrove DE, Gunter TE. Kinetics of mitochondrial calcium transport. II. A kinetic description of the sodium-dependent calcium efflux mechanism of liver mitochondria and inhibition by ruthenium red and by tetraphenylphosphonium. J Biol Chem. 1986;261:15166–71.

67. Pradhan RK, Beard DA, Dash RK. A Biophysically Based Mathematical Model for the Kinetics of Mitochondrial Na+-Ca2+ Antiporter. Biophys J. 2010;98:218–30.

68. Kummer U, Olsen LF, Dixon CJ, Green AK, Bornberg-Bauer E, Baier G. Switching from Simple to Complex Oscillations in Calcium Signaling. Biophys J. 2000;79:1188–95.

69. Catterall WA. Voltage-Gated Calcium Channels. Cold Spring Harb Perspect Biol. 2011;3:a003947–a003947.

70. Chay TR, Keizer J. Minimal model for membrane oscillations in the pancreatic beta-cell. Biophys J. 1983;42:181–9.

71. LeBeau AP, Van Goor F, Stojilkovic SS, Sherman A. Modeling of Membrane Excitability in Gonadotropin-Releasing Hormone-Secreting Hypothalamic Neurons Regulated by Ca $^{2+}$ -Mobilizing and Adenylyl Cyclase-Coupled Receptors. J Neurosci. 2000;20:9290–7.

72. Destexhe A, Huguenard JR. Nonlinear Thermodynamic Models of Voltage-Dependent Currents.

73. Keynes RD. The Ionic Channels in Excitable Membranes. In: Wolstenholme GEW, Fitzsimons DW, editors. Novartis Found Symp [Internet]. Chichester, UK: John Wiley & Sons, Ltd.; 2008 [cited 2023 Jun 22]. p. 191–203. Available from: https://onlinelibrary.wiley.com/doi/10.1002/9780470720134.ch11

74. Croisier H, Tan X, Perez-Zoghbi JF, Sanderson MJ, Sneyd J, Brook BS. Activation of Store-Operated Calcium Entry in Airway Smooth Muscle Cells: Insight from a Mathematical Model. Csernoch L, editor. PLoS ONE. 2013;8:e69598.

75. Ong HL, Liu X, Tsaneva-Atanasova K, Singh BB, Bandyopadhyay BC, Swaim WD, et al. Relocalization of STIM1 for Activation of Store-operated Ca2+ Entry Is Determined by the Depletion of Subplasma Membrane Endoplasmic Reticulum Ca2+ Store. J Biol Chem. 2007;282:12176–85.

76. Hoover PJ, Lewis RS. Stoichiometric requirements for trapping and gating of Ca $^{2+}$ release-activated Ca $^{2+}$ (CRAC) channels by stromal interaction molecule 1 (STIM1). Proc Natl Acad Sci. 2011;108:13299–304.

77. Sneyd J, Falcke M. Models of the inositol trisphosphate receptor. Prog Biophys Mol Biol. 2005;89:207–45.

78. Yang F, Huang L, Tso A, Wang H, Cui L, Lin L, et al. Inositol 1,4,5-trisphosphate receptors are essential for fetal-maternal connection and embryo viability. Firulli AB, editor. PLOS Genet. 2020;16:e1008739.

79. Dupont G, Combettes L. Modelling the effect of specific inositol 1,4,5-trisphosphate receptor isoforms on cellular Ca2+ signals. Biol Cell. 2006;98:171–82.

80. Hagar RE, Burgstahler AD, Nathanson MH, Ehrlich BE. Type III InsP3 receptor channel stays open in the presence of increased calcium. Nature. 1998;396:81–4.

81. Siekmann I, Wagner LE, Yule D, Crampin EJ, Sneyd J. A Kinetic Model for Type I and II IP3R Accounting for Mode Changes. Biophys J. 2012;103:658–68.

82. Keizer J, De Young GW. Two roles of Ca2+ in agonist stimulated Ca2+ oscillations. Biophys J. 1992;61:649–60.

83. Li Y-X, Rinzel J. Equations for InsP3 Receptor-mediated [Ca2+]i Oscillations Derived from a Detailed Kinetic Model: A Hodgkin-Huxley Like Formalism. J Theor Biol. 1994;166:461–73.

84. Endo M, Tanaka M, Ogawa Y. Calcium Induced Release of Calcium from the Sarcoplasmic Reticulum of Skinned Skeletal Muscle Fibres. Nature. 1970;228:34–6.

85. Friel DD. [Ca2+]i oscillations in sympathetic neurons: an experimental test of a theoretical model. Biophys J. 1995;68:1752–66.

86. Schuster S, Marhl M, Höfer T. Modelling of simple and complex calcium oscillations: From single-cell responses to intercellular signalling. Eur J Biochem. 2002;269:1333–55.

87. Wacquier B, Combettes L, Van Nhieu GT, Dupont G. Interplay Between Intracellular Ca2+ Oscillations and Ca2+-stimulated Mitochondrial Metabolism. Sci Rep. 2016;6:19316.

88. Sneyd J, Han JM, Wang L, Chen J, Yang X, Tanimura A, et al. On the dynamical structure of calcium oscillations. Proc Natl Acad Sci. 2017;114:1456–61.

89. Han JM, Tanimura A, Kirk V, Sneyd J. A mathematical model of calcium dynamics in HSY cells. McCulloch AD, editor. PLOS Comput Biol. 2017;13:e1005275.

90. Singh N, Adlakha N. A mathematical model for interdependent calcium and inositol 1,4,5-trisphosphate in cardiac myocyte. Netw Model Anal Health Inform Bioinforma. 2019;8:18.

91. Dave DD, Jha BK. Mathematical Modeling of Calcium Oscillatory Patterns in a Neuron. Interdiscip Sci Comput Life Sci. 2021;13:12–24.

92. Chang Y, Funk M, Roy S, Stephenson E, Choi S, Kojouharov HV, et al. Developing a Mathematical Model of Intracellular Calcium Dynamics for Evaluating Combined Anticancer Effects of Afatinib and RP4010 in Esophageal Cancer. Int J Mol Sci. 2022;23:1763.

93. Panetta JC, Schaiquevich P, Santana VM, Stewart CF. Using Pharmacokinetic and Pharmacodynamic Modeling and Simulation to Evaluate Importance of Schedule in Topotecan Therapy for Pediatric Neuroblastoma. Clin Cancer Res. 2008;14:318–25.

94. He Y, Kodali A, Wallace DI. Predictive Modeling of Neuroblastoma Growth Dynamics in Xenograft Model After Bevacizumab Anti-VEGF Therapy. Bull Math Biol. 2018;80:2026–48.

95. Otero JG, Alcamí AÁ-A, Belmonte-Beitia J. Dynamics and analysis of a mathematical model of neuroblastoma treated with Celyvir. Appl Math Model. 2022;110:131–48.

96. Swan GW. Role of optimal control theory in cancer chemotherapy. Math Biosci. 1990;101:237–84.

97. Świerniak A, Kimmel M, Smieja J, Puszynski K, Psiuk-Maksymowicz K. Cell Cycle as an Object of Control. Syst Eng Approach Plan Anticancer Ther [Internet]. Cham: Springer International Publishing; 2016 [cited 2023 Jun 22]. p. 9–54. Available from: http://link.springer.com/10.1007/978-3-319-28095-0_2

98. Chaffey N. Alberts, B., Johnson, A., Lewis, J., Raff, M., Roberts, K. and Walter, P. Molecular biology of the cell. 4th edn. Ann Bot. 2003;91:401–401.

99. Borys D, Jaksik R, Krześlak M, Śmieja J, Świerniak A. Cancer—A Story on Fault Propagation in Gene-Cellular Networks. In: Król D, Fay D, Gabryś B, editors. Propag Phenom Real World Netw [Internet]. Cham: Springer International Publishing; 2015 [cited 2023 Jun 22]. p. 225–56. Available from: https://link.springer.com/10.1007/978-3-319-15916-4_10

100. Wacquier B, Combettes L, Van Nhieu GT, Dupont G. Interplay Between Intracellular Ca2+ Oscillations and Ca2+-stimulated Mitochondrial Metabolism. Sci Rep. 2016;6:19316.

101. Wallace DI, Dunham A, Chen PX, Chen M, Huynh M, Rheingold E, et al. A Model for Spheroid versus Monolayer Response of SK-N-SH Neuroblastoma Cells to Treatment with 15-Deoxy- *PGJ* $_2$. Comput Math Methods Med. 2016;2016:1–11.

102. Pande G, Kumar NA, Manogaran PS. Flow cytometric study of changes in the intracellular free calcium during the cell cycle. Cytometry. 1996;24:55–63.

103. Panetta JC, Fister KR. Optimal Control Applied to Cell-Cycle-Specific Cancer Chemotherapy. SIAM J Appl Math. 2000;60:1059–72.

104. Clare SE, Nakhlis F, Panetta JC. Molecular biology of breast metastasis The use of mathematical models to determine relapse and to predict response to chemotherapy in breast cancer. Breast Cancer Res. 2000;2:430.

105. Komarova NL, Wodarz D. Effect of Cellular Quiescence on the Success of Targeted CML Therapy. Agur Z, editor. PLoS ONE. 2007;2:e990.

106. Wacquier B, Combettes L, Van Nhieu GT, Dupont G. Interplay Between Intracellular Ca2+ Oscillations and Ca2+-stimulated Mitochondrial Metabolism. Sci Rep. 2016;6:19316.

107. Baldi C, Vazquez G, Boland R. Capacitative calcium influx in human epithelial breast cancer and non-tumorigenic cells occurs through Ca2+ entry pathways with different permeabilities to divalent cations. J Cell Biochem. 2003;88:1265–72.

108. Motiani RK, Hyzinski-García MC, Zhang X, Henkel MM, Abdullaev IF, Kuo Y-H, et al. STIM1 and Orai1 mediate CRAC channel activity and are essential for human glioblastoma invasion. Pflüg Arch - Eur J Physiol. 2013;465:1249–60.

109. Umemura M, Baljinnyam E, Feske S, De Lorenzo MS, Xie L-H, Feng X, et al. Store-operated Ca2+ entry (SOCE) regulates melanoma proliferation and cell migration. PloS One. 2014;9:e89292.

110. Zhu H, Zhang H, Jin F, Fang M, Huang M, Yang CS, et al. Elevated Orai1 expression mediates tumor-promoting intracellular Ca2+ oscillations in human esophageal squamous cell carcinoma. Oncotarget. 2014;5:3455–71.

111. Stewart TA, Yapa KTDS, Monteith GR. Altered calcium signaling in cancer cells. Biochim Biophys Acta BBA - Biomembr. 2015;1848:2502–11.

112. Fulda S, Honer M, Menke-Moellers I, Berthold F. Antiproliferative potential of cytostatic drugs on neuroblastoma cells in vitro. Eur J Cancer. 1995;31:616–21.

113. Seifrtová M, Havelek R, Chmelařová M, Cmielová J, Muthná D, Stoklasová A, et al. The effect of ATM and ERK1/2 inhibition on mitoxantrone-induced cell death of leukaemic cells. Folia Biol (Praha). 2011;57:74–81.

114. Fox EJ. Mechanism of action of mitoxantrone. Neurology. 2004;63:S15–8.

115. Iversen OH, Clausen OPF, Iversen UM, Rohrbach R. SOME EFFECTS OF BLEOMYCIN ON THE PROLIFERATION, MATURATION TIME and PROTEIN SYNTHESIS OF HAIRLESS MOUSE EPIDERMIS. Cell Prolif. 1976;9:77–97.

116. Tchounwou PB, Dasari S, Noubissi FK, Ray P, Kumar S. Advances in Our Understanding of the Molecular Mechanisms of Action of Cisplatin in Cancer Therapy. J Exp Pharmacol. 2021;Volume 13:303–28.

117. van der Vijgh WJF. Clinical Pharmacokinetics of Carboplatin: Clin Pharmacokinet. 1991;21:242–61.

118. Weiss MA, Aliff TB, Tallman MS, Frankel SR, Kalaycio ME, Maslak PG, et al. A single, high dose of idarubicin combined with cytarabine as induction therapy for adult patients with recurrent or refractory acute lymphoblastic leukemia. Cancer. 2002;95:581–7.

119. Simsek M, Deben DS, Horjus CS, Bénard MV, Lissenberg-Witte BI, Buiter HJC, et al. Sustained effectiveness, safety and therapeutic drug monitoring of tioguanine in a cohort of 274 IBD patients intolerant for conventional therapies. Aliment Pharmacol Ther. 2019;50:54–65.

120. Furlanut M, Franceschi L. Pharmacology of Ifosfamide. Oncology. 2003;65:2–6.

121. Balis FM, Holcenberg JS, Poplack DG, Ge J, Sather HN, Murphy RF, et al. Pharmacokinetics and Pharmacodynamics of Oral Methotrexate and Mercaptopurine in Children With Lower Risk Acute Lymphoblastic Leukemia: A Joint Children's Cancer Group and Pediatric Oncology Branch Study. Blood. 1998;92:3569–77.

122. Wick W, Gorlia T, Bendszus M, Taphoorn M, Sahm F, Harting I, et al. Lomustine and Bevacizumab in Progressive Glioblastoma. N Engl J Med. 2017;377:1954–63.

123. Yung WKA, Albright RE, Olson J, Fredericks R, Fink K, Prados MD, et al. A phase II study of temozolomide vs. procarbazine in patients with glioblastoma multiforme at first relapse. Br J Cancer. 2000;83:588–93.

124. Nath R, Raser K, Hajimohammadreza I, Wang K. Thapsigargin induces apoptosis in SH-SY5Y neuroblastoma cells and cerebrocortical cultures. IUBMB Life. 1997;43:197–205.

125. Dahmer MK. Caspases-2, -3, and -7 are involved in thapsigargin-induced apoptosis of SH-SY5Y neuroblastoma cells. J Neurosci Res. 2005;80:576–83.

126. Sehgal P, Szalai P, Olesen C, Praetorius HA, Nissen P, Christensen SB, et al. Inhibition of the sarco/endoplasmic reticulum (ER) Ca2+-ATPase by thapsigargin analogs induces cell death via ER Ca2+ depletion and the unfolded protein response. J Biol Chem. 2017;292:19656–73.

127. Akhtar N, Jabeen I. A 2D-QSAR and Grid-Independent Molecular Descriptor (GRIND) Analysis of Quinoline-Type Inhibitors of Akt2: Exploration of the Binding Mode in the Pleckstrin Homology (PH) Domain. Maga G, editor. PLOS ONE. 2016;11:e0168806.